Nuclear Instruments and Methods in Physics Research A297 (1990) 60–86
North-Holland

A verified upgrade of the GHEISHA 6/7 simulation of particle interactions

Zbigniew Jakubowski *
Deutsches Elektronen, Synchrotron, Hamburg, FRG

Michael Kobel
Universität Erlangen-Nürnberg, FRG

Received 6 July 1990

We propose changes in the GHEISHA 6/7 code concerning the simulation of energy loss of charged particles, δ-rays, multiple scattering, negative particle absorption, light quenching in scintillators, and neutron capture. These changes have a profound theoretical motivation and are supported by comparing the resulting detector simulation with Crystal Ball data.

1. Introduction

Uncertainties in the simulation of the detector response are one of the main sources of systematic errors in the analysis of high energy physics experiments. Improvements in the detector simulation would increase the precision of measurements and thus open new possibilities to measure more subtle effects. Even though each experiment has to select the most appropriate Monte Carlo simulation program for its own detector, the physics under study, and the available computer resources, there are a few program packages of which at least some parts are used in most experiments. In the following we will report on proposed improvements for one of these codes, the GHEISHA package [1], which stands for Gamma, Hadron, and Electron Interaction and SHower Algorithm.

In the sections 2 and 3 some substantial modifications are proposed for the GHEISHA 6/7 simulation program, which are expected to be of importance for calorimetric devices or high precision energy loss measurements. Since many of our changes to GHEISHA are motivated by the observation that the applied formulae differ from the exact theory, we will review the results of the theory of energy loss, δ-rays, and multiple scattering in section 2.1 and list the formulae applied by GHEISHA 6/7 in section 2.2. Section 2.3 will introduce μ-pair data samples for testing these interactions, and describe their Monte Carlo modeling. In section 2.4 we will list our changes to the corresponding GHEISHA routines and discuss their influence on the simulation.

The complexity and variety of hadronic interactions in a calorimeter requires to start investigating this part of the GHEISHA code with the help of real data rather than from the theoretical side. In section 3.1 a careful interpretation of discrepancies between the measured and the simulated distributions of event shape variables of multihadron events allows us to find out the interaction processes crucial for the correct simulation of these variables. An inspection of the corresponding GHEISHA routines reveals shortcomings in the modeling of negative particle absorption, light quenching, and neutron capture. Our improvements to these issues will be discussed in section 3.2.

In section 4 we summarize our results and present our conclusions.

2. Simulation of energy loss

In the following we will confront the GHEISHA simulation of energy loss with theory and data, propose changes, and show the resulting improvements in the reproduction of the data.

2.1. Energy loss of charged particles

All visible energy in a calorimeter is deposited via the energy loss of charged particles, regardless whether these particles come from the primary interaction or from secondary processes in the detector. A proper

* On leave from Institute of Nuclear Physics, Cracow, Poland.

0168-9002/90/$03.50

description of these electromagnetic processes is a fundamental basis for the simulation of any kind of interaction. For the identification of primary particles, the knowledge of the expected energy loss in a given detector component is often necessary to percent accuracy.

We first review the results of the theory of energy loss, δ-rays, and scattering in order to provide a basis for the examination of the corresponding GHEISHA routines. We restrict ourselves to incident charged particles other than e^- and e^+. Following the above arguments, we must not neglect corrections which may influence the energy loss predictions by a few percent.

The amount of energy lost by excitation and ionization of the atoms can be quantified in three different ways, which will be discussed in the following sections, namely the mean energy loss, the restricted energy loss, and the most probable energy loss.

2.1.1. The mean energy loss

The mean energy loss includes all energy transfers T_e to the atomic electrons up to the kinematic limit T_e^{max} (see eq. (3)). It is expressed by the Bethe–Bloch formula [2,3], extended by the density effect correction δ:

$$-\left(\frac{dE}{dx}\right)_{mean} = D\frac{Q^2}{\beta^2}\left[\ln\left(\frac{2m_ec^2T_e^{max}}{I^2}\beta^2\gamma^2\right) - 2\beta^2 - \delta\right]. \quad (1)$$

Here and in the following the values without a subscript refer to the incident particle whereas the subscript e denotes the atomic electrons. The kinematic variables of the particles are parametrized by $\beta = v/c$ and $\gamma = E/mc^2$, Q is the electric charge in units of e, I is the mean ionization potential, and D is proportional to the electron density n_e of the traversed medium:

$$D = \frac{2\pi e^4}{m_ec^2}n_e = 0.1536\ \text{MeV/cm}\left(\frac{\rho}{\text{g/cm}^3}\frac{Z}{A}\right). \quad (2)$$

Here ρ is the density and Z/A is the ratio of the charge to the mass number of the medium. For compounds one has to replace this ratio by $\langle Z\rangle/\langle A\rangle$. The density effect correction δ will be described in more detail in subsection 2.1.5.

The validity of formula (1) is limited on the low energy side by a correction term for nonrelativistic particle velocities, the so-called shell correction for velocities of the order of those of the bound electrons in the medium. For highly relativistic particles with $\beta\gamma = O(m/m_e)$ corrections arise from the rate of energy transfers near T_e^{max}, which then deviates from eq. (7). In addition the energy loss via bremsstrahlung and pair production becomes increasingly important at those high energies.

The value of the expression in the square brackets lies for the majority of applications between 10 and 40. To estimate the influence of several corrections to the energy loss formula, we will assume a value of 20 hereafter.

2.1.2. The δ-rays

The shape of the energy loss distribution is in general not purely Gaussian, but rather a Landau distribution showing a tail towards higher energy losses. This is due energy transfers to single electrons much greater than their typical binding energy. These electrons are called knock-on electrons or δ-rays.

The detailed shape of the tail, however, depends strongly on the layer thickness and the incident particle energy: Only those δ-rays contribute to the tail, which have energies greater than the width of the Gaussian part of the distribution, which in turn depends on the layer thickness. In addition the maximum kinetic energy of knock-on electrons is given by

$$T_e^{max} = \frac{2m_ec^2\beta^2\gamma^2}{1 + 2\gamma\frac{m_e}{m} + \left(\frac{m_e}{m}\right)^2} \quad (3)$$

and thus depends on the incident particle energy. The δ-ray electrons are ejected under an angle θ with respect to the incident particle direction which is obtained from 4-momentum conservation:

$$\cos\theta = \frac{(E + m_ec^2)(E_e - m_ec^2)}{pp_e} = \left(1 + \frac{m_e}{\gamma m}\right)\frac{1}{\beta}\sqrt{\frac{T_e}{T_e + 2m_ec^2}} \approx \frac{1}{\beta}\sqrt{\frac{T_e}{T_e + 2m_ec^2}}. \quad (4)$$

For $\gamma \ll m/2m_e$ the maximum δ-ray energy reduces to

$$T_e^{max} = 2m_ec^2\beta^2\gamma^2. \quad (5)$$

Thus for nonrelativistic particle momenta ($\beta\gamma \approx \beta \ll 1$) $T_e \ll 2m_ec^2$ holds for all T_e, and we get in the low momentum limit in agreement with the result of ref. [4]:

$$\cos\theta = \sqrt{\frac{T_e}{T_e^{max}}}. \quad (6)$$

The number N_e of δ-rays produced with energy T_e in a given thickness dx has been calculated in the years 1938–1940 under the assumption of heavy pointlike particles and free electrons [5]:

$$\frac{d^2N_e}{dx\,dT_e} = D\frac{Q^2}{\beta^2}\frac{1}{T_e^2}\left(1 - \beta^2\frac{T_e}{T_e^{max}}\right). \quad (7)$$

This formula is exact for spinless particles only. The spin-dependent terms are small except for $T_e \gg mc^2$.

(For 5 GeV muons they increase the value of the bracket by only 0.0005 at $T_e = 150$ MeV, but already about 0.05 at $T_e = T_e^{max} = 1.5$ GeV, approaching 0.5 for higher energetic muons and maximum energy transfer.)

The energy transfer to δ-rays above a limit T_e^0 is obtained by integrating the above expression:

$$-\left(\frac{dE}{dx}\right)_{T_e > T_e^0} = \int_{T_e^0}^{T_e^{max}} T_e \frac{d^2N_e}{dx\, dT_e} dT_e = D\frac{Q^2}{\beta^2}\left[\ln\frac{T_e^{max}}{T_e^0} - \beta^2\left(1 - \frac{T_e^0}{T_e^{max}}\right)\right]. \quad (8)$$

2.1.3. The restricted energy loss

The restricted energy loss is defined as the mean energy loss including all single energy transfers below a limit T_e^0. It is the relevant quantity, if δ-rays above an energy T_e^0 are not measured or treated in a special way, e.g. if they escape a given detector component.

It is usually cited [6,13] in the limit $T_e^0 \ll T_e^{max}$ as it was found by Bethe [2] in the derivation of the formula for the mean energy loss (1). We now deduce it from a reverse procedure, namely by subtracting the amount of energy transfered above T_e^0 (eq. (8)) from the mean energy loss (1), yielding.

$$-\left(\frac{dE}{dx}\right)_{T_e < T_e^0} = D\frac{Q^2}{\beta^2}\left[\ln\left(\frac{2m_e c^2 T_e^0}{I^2}\beta^2\gamma^2\right) - \beta^2\left(1 + \frac{T_e^0}{T_e^{max}}\right) - \delta\right] \quad (9)$$

Compared to the result of Bethe our formula reveals an additional factor $(1 + T_e^0/T_e^{max})$, which extends the validity of eq. (9) to all $T_e^0 \le T_e^{max}$ provided that T_e^0 is large compared to the electron binding energies, and creates a smooth continuation of the restricted energy loss into the mean energy loss (1) at $T_e^0 = T_e^{max}$. The factor reduces for $T_e^0 \lesssim T_e^{max}$ the calculated value for the restricted energy loss by up to ~ 5%. Propagating the spin-dependent terms, neglected in eq. (7), would affect the result by less than 0.1% for T_e^0 below 1 GeV.

2.1.4. The most probable energy loss

If the energy loss distribution is not Gaussian, the most probable energy loss $(\Delta E)_{mp}$ in a given layer Δx differs from $(dE/dx)_{mean}\Delta x$. According to Landau [7] the most probable energy loss is approximately given by the restricted energy loss of eq. (9), if the cutoff parameter T_e^0 is chosen to be

$$T_e^0 = \xi \equiv D\frac{Q^2}{\beta^2}\Delta x \quad (10)$$

yielding

$$-(\Delta E)_{mp} = \xi\left[\ln\left(\frac{2m_e c^2 \xi}{I^2}\beta^2\gamma^2\right) - \beta^2 + 0.198 - \delta\right]. \quad (11)$$

The contribution of energy transfers greater than ξ to the most probable energy loss value is accounted for by the numerical correction term 0.198, which raises the peak position generally by about 1%. The final value of this term was determined by Maccabee and Papworth [8]. Formula (11) is only valid for thin layers such that $\xi/T_e^{max} < 0.05$ and $(\Delta E)_{mp} \ll T$, where T is the kinetic energy of the incident particle. Provided the first condition is fulfilled, the latter one is implied for $\beta\gamma \lesssim 10$.

The physical meaning of ξ can be deduced from the expression for the produced number of δ-rays above T_e^0 in Δx:

$$\Delta N_e(T_e \ge T_e^0) = \Delta x \int_{T_e^0}^{T_e^{max}} \frac{d^2N_e}{dx\, dT_e} dT_e = D\frac{Q^2}{\beta^2}\Delta x\left(\frac{1}{T_e^0} - \frac{1}{T_e^{max}}\left(1 + \beta^2 \ln\frac{T_e^{max}}{T_e^0}\right)\right) \approx \frac{\xi}{T_e^0} \quad \text{for } T_e^0 \ll T_e^{max}, \quad (12)$$

i.e. on an average there is one δ-ray produced above an energy ξ. Simply spoken, the δ-rays below ξ contribute merely to the energy loss peak position $(\Delta E)_{mp}$, whereas the δ-rays above ξ create the tail of the Landau distribution.

2.1.5. The density effect correction

It is well known, that the restricted (eq. (9)) and the most probable (eq. (11)) energy loss via ionization and excitation reach a saturation for highly relativistic particles. It has its origin in the polarization of the medium by the incident particle and is called density effect. The mean energy loss, however, keeps increasing, since the rising maximum energy transfer T_e^{max} (see eq. (3)) to single δ-ray electrons extends the tail of the Landau distribution to higher energies.

After a first suggestion by Swann [9] in 1938 an analytic expression for the density effect was derived by Fermi [10], which still suffered from the incomplete knowledge of the dispersion law affecting the $\beta\gamma$ and material dependence in the region below saturation. Sternheimer introduced a method [11] to calculate the functional dependence of $\delta(\beta\gamma)$ numerically from the measured values of the mean ionization potential I and the atomic absorption edges $\hbar\omega_i$. Throughout the years 1952–1984 Sternheimer [11–15] obtained results for an enormous number of materials. (In the most recent publication [15] the correction parameters for a total of

278 substances are given.) The numerical results of $\delta(\beta\gamma)$ were fitted for each material by the following empirical expression involving the Sternheimer parameters $\bar{C}$, b, n, Y_0, and Y_1 *:

$$\begin{aligned} &\delta = 0 && \text{for} \quad \beta\gamma \le Y_0, \\ &\delta = \ln \beta^2\gamma^2 - \bar{C} + b\left(\ln\frac{Y_1}{\beta\gamma}\right)^n && \text{for} \quad Y_0 < \beta\gamma < Y_1, \\ &\delta = \ln \beta^2\gamma^2 - \bar{C} && \text{for} \quad Y_1 \le \beta\gamma. \end{aligned} \tag{13}$$

The exponent n is found to be close to 3 for most materials. The boundary momenta of the transition range between the uncorrected energy loss without density effect and the saturation value are formed by the parameters Y_0 and Y_1. The boundary condition at $\beta\gamma = Y_0$ fixes the parameter b to

$$b = \left(\bar{C} - \ln Y_0^2\right)\left(\ln\frac{Y_1}{Y_0}\right)^{-n}. \tag{14}$$

Finally, the parameter $\bar{C}$ is given by the fact that for very high energies the energy loss no longer depends on the mean ionization potential I but merely on the electron density n_e [10], expressed in terms of the electron plasma frequency ω_p. The theory yields the following expression for $\bar{C}$ which cancels the I dependence of all three energy loss formulas for $\beta\gamma > Y_1$:

$$\bar{C} = 2\ln\left(\frac{I}{\hbar\omega_p}\right) + 1, \tag{15}$$

where $\hbar\omega_p$ is given by

$$\hbar\omega_p = \left(2m_e c^2 D a_0\right)^{1/2} = 28.8\ \text{eV}\left(\frac{\rho}{\text{g/cm}^3}\frac{Z}{A}\right)^{1/2} \tag{16}$$

and $a_0 = \hbar^2/e^2 m_e$ is the Bohr radius.

Using eqs. (13) and (15) the saturation value of the restricted energy loss becomes

$$\begin{aligned} -\lim_{\beta\gamma\to\infty}\left(\frac{dE}{dx}\right)_{T_e<T_e^0} &= DQ^2\ln\left(\frac{2m_e c^2 T_e^0}{(\hbar\omega_p)^2}\right) \\ &= DQ^2\ln\left(\frac{T_e^0}{Da_0}\right) = \text{const}. \end{aligned} \tag{17}$$

The only material parameter entering via D is the electron density.

* In comparison to the original Sternheimer parametrization using the parameters C, a, m, X_0, X_1 our parameter set $\bar{C}$, b, n, Y_0, Y_1 is defined by: $\bar{C} = -C$, $b = a/(\ln 10)^m$, $n = m$, $Y_0 = 10^{X_0}$, $Y_1 = 10^{X_1}$.

Table 1
Calculated and measured mean ionization potentials I (in eV). For compounds, $\langle Z\rangle$ was used in eq. (19)

	Material						
	Al	Fe	Cu	Pb	U	NaI	BGO
Formula (19)	163	285	314	826	923	343	439
Measured [15]	166	286	322	823	890	452	534

In the intermediate range $Y_0 < \beta\gamma < Y_1$ the restricted energy loss reads:

$$\begin{aligned} &-\left(\frac{dE}{dx}\right)_{T_e<T_e^0}^{Y_0<\beta\gamma<Y_1} \\ &= D\frac{Q^2}{\beta^2}\left[\ln\left(\frac{T_e^0}{Da_0}\right) + 1 - \beta^2\left(1 + \frac{T_e^0}{T_e^{\max}}\right) - b\left(\ln\frac{Y_1}{\beta\gamma}\right)^n\right]. \end{aligned} \tag{18}$$

The momentum dependence is governed by the Sternheimer parameters Y_0, Y_1, and n, which depend on the absorption edges of the atomic spectra. For solids and liquids the above expression covers the most important momentum range for typical high energy physics experiments, since the fit yields Y parameters in the range $1 \le Y_0 \le 3$ and $10^2 \le Y_1 \le 10^3$. For gases Sternheimer finds values of $40 \le Y_0 \le 100$ and $10^4 \le Y_1 \le 10^5$.

Since the fitting procedure has to be performed for each material separately, we call the result the density effect expression from material fits. Its inherent errors are expressed in ref. [15] by quoting the maximum deviations at any point between the fitted expression and the numerical values of δ. For the various materials they lie between 0.02 and 0.12 corresponding to errors of the energy loss ranging from 0.1% to 0.6%.

In 1971 Sternheimer introduced a general expression for the density effect [13] valid for all materials but H_2 and He. It expresses all parameters as a function of $\bar{C}$ and the aggregate state of the medium. Since $\bar{C}$ in turn depends only on I and n_e, it opened the opportunity to derive the energy loss dE/dx completely without numerically calculating and fitting $\delta(\beta\gamma)$ for the given material, but rather using I and n_e as an input. This "general expression" is expected to be accurate for dE/dx to about 1% with a maximum error of less than 2% over the whole momentum range.

In order to facilitate the calculation of $\delta(\beta\gamma)$ even more, Sternheimer proposed the following approximation [12] for the mean ionization potential I of materials with $Z \ge 13$:

$$I = \left(9.76Z + \frac{58.8}{Z^{0.19}}\right)\text{eV}. \tag{19}$$

As can be seen from table 1 the results of this expression match very well with the measured values from ref.

[15] as far as pure elements are concerned. However, there may be substantial differences for compounds, if one uses for Z simply the arithmetic mean $\langle Z\rangle$ (see table 1). For the two compounds listed, this would introduce errors of the order of 2% in the calculation of dE/dx. The differences become somewhat smaller, if one inserts the geometric mean of the components' ionization potentials $\ln I = \langle Z \ln I\rangle/\langle Z\rangle$ rather than a mean Z value.

2.1.6. Single, plural, and multiple scattering

Charged particles traversing a finite material thickness Δx undergo elastic scattering in the Coulomb fields of the nuclei. The number of scatters Ω with a scattering angle χ, defined as the angle in space between the directions before and after the scatter, is given by the Rutherford result in the small angle approximation

$$\frac{d\Omega}{d\chi} = \frac{2\chi_c^2}{\chi^3}, \tag{20}$$

where the square of the characteristic scattering angle χ_c is

$$\chi_c^2 = 4\pi e^4 n_n \Delta x \frac{Z^2Q^2}{p^2v^2} = 2D\frac{Q^2}{\beta^2}\Delta x\frac{Zm_e}{p^2} \tag{21}$$

and n_n denotes the number of nuclei per volume. For compounds the replacements $Z^2 = \langle Z^2\rangle$, and $DZ \propto \langle Z^2\rangle/\langle A\rangle$ have to be made, respectively.

The validity of the Rutherford result is limited for small χ by the screening of the atomic electrons. Using the ansatz $V(r) = (QZe^2/r)\exp(-r/r_\mu)$ for the screened potential, a minimum scattering angle χ_μ can be defined by

$$\chi_\mu = \frac{\hbar}{pr_\mu}. \tag{22}$$

The screening radius r_μ is usually chosen to equal within a factor of 2 the Thomas–Fermi radius r_0. The uncertainty is expressed with the help of a scale factor μ:

$$r_\mu = \frac{r_0}{\mu} = \frac{0.885}{\mu Z^{1/3}}a_0. \tag{23}$$

For compounds $Z^{1/3}$ has to be replaced by the weighted geometric mean obtained from $\ln Z^{1/3} = \langle Z^2 \ln Z^{1/3}\rangle/\langle Z^2\rangle$. The maximum scattering angle χ_ν above which nuclear form factors considerably reduce the elastic Coulomb scattering probability is given by the size r_ν of the nuclei

$$\chi_\nu = \frac{\hbar}{pr_\nu}, \tag{24}$$

which can be conveniently parametrized as

$$r_\nu = \nu\frac{e^2}{m_e c^2}A^{1/3}. \tag{25}$$

Using $r_\nu = 1.13$ fm $A^{1/3}$ [16] results in $\nu = 0.40$.

Since $\chi_\mu/\chi_\nu \approx \alpha^2(ZA)^{1/3} \ll 1$, where $\alpha = e^2/\hbar c$ is the QED coupling constant, the total number of scatters Ω_0 above χ_μ can be obtained by integrating expression (20) from χ_μ to infinity:

$$\Omega_0 = \int_{\chi_\mu}^{\infty}\frac{d\Omega}{d\chi}d\chi = \frac{\chi_c^2}{\chi_\mu^2}$$
$$= 2D\frac{Q^2}{\beta^2}\Delta x\frac{Z}{m_e c^2\alpha^2}\left(\frac{r_\mu}{a_0}\right)^2$$
$$= 2730\frac{Q^2}{\beta^2}\frac{\rho\Delta x}{\mathrm{g/cm^2}}\frac{Z^{4/3}}{A} \quad \text{for} \quad \mu = 1.8\ [17]. \tag{26}$$

Given the large uncertainty in the value of μ (compare the lower values in refs. [18]), it is sufficiently accurate here to simply insert for compounds their mean Z and A values.

For $\rho\Delta x \gtrsim 0.1$ g/cm^2 the value $\Omega_0 \gtrsim 200$ implies that multiple scattering under small angles does occur. It can be quantified most transparently by the total scattering angle projected on two perpendicular planes containing the incident particle direction (referred to as the projected angles θ and ϕ) and the projected displacements y and z in these two planes. The projected angles are Gaussian distributed for small angles

$$p(\eta)\,d\eta \approx \sqrt{\frac{2}{\pi}}\,e^{-\eta^2/2}\,d\eta. \tag{27}$$

Here $\eta \equiv |\theta/\theta_0|$ or $\eta \equiv |\phi/\phi_0|$, respectively, is the reduced projected scattering angle, and $\theta_0 = \phi_0$ is the width of the Gaussian distributions *. The Molière theory [19] of multiple scattering yields

$$\theta_0^2 = \chi_c^2\frac{B}{2}, \tag{28}$$

where the Molière B parameter can be obtained from the transcendent equation

$$B - \ln B = \ln\Omega_0 - 0.1544 \tag{29}$$

and 0.1544 is twice the Euler constant minus 1. Scott [20] gives an approximate solution

$$B = 1.153 + 2.583\log_{10}\Omega_0, \tag{30}$$

which is accurate to 0.5% for Ω_0 in the range between 10^2 and 10^5, and to 3% up to $\Omega_0 = 10^9$.

For scattering angles larger than about $2.5\theta_0$ the Gaussian probability does not hold, since this region is governed by plural scattering. Further away single scattering dominates, and the probability distribution

* Note the difference of $\sqrt{2}$ in our definition of η, θ_0, and ϕ_0 compared to other authors using $p(\eta) \propto \exp(-\eta^2)$.

approaches the Rutherford result of eq. (20), which reads in terms of the reduced projected angle

$$p(\eta)\,\mathrm{d}\eta = \frac{4}{B}\frac{\mathrm{d}\eta}{\eta^3}. \tag{31}$$

The small angle approximation is justified as long as $\chi_\nu \lesssim 1$ implying $p \gtrsim 175\ \mathrm{MeV}/c\ A^{-1/3}$.

Eq. (31), together with eqs. (30), (26), and (27), shows that the relative amount of single scattering to multiple scattering is nearly independent of the incident particle momentum (as long as $\beta \approx 1$), and only weakly sensitive to the type of nuclei (via $\log_{10}(Z^{4/3}/A)$). However, it varies logarithmically with the material thickness $\rho\Delta x$, which may span several orders of magnitude in different applications. The latter is a consequence of the thickness dependence of the characteristic scattering angle χ_c, featuring that only one single scatter larger than χ_c occurs in a given material layer. The range of single scattering angles χ, contributing to multiple scattering and determining the width of its Gaussian distribution, is limited through χ_c and thus depends on $\rho\Delta x$. If the root mean square angle of all single scattering angles up to the maximum angle χ_ν is mistaken as the width of the Gaussian, like in ref. [21], the results on the relative amount of single scattering becomes incorrect and the logarithmic dependence on the material thickness disappears. Note, that eqs. (31) and (27) include a factor of 2 due to restricting η to positive values in our definition *. In addition the factor $\sqrt{2/\pi}$ in eq. (27) has to be slightly modified to guarantee the overall normalization of $p(\eta)$.

A strong material dependence, however, may be introduced via the maximum scattering angle χ_ν. The single scattering tail extends only up to η_{max}, which is defined from the above equations by

$$\frac{1}{\eta_{max}} \equiv \frac{\theta_0}{\chi_\nu} = \frac{\chi_\mu}{\chi_\nu}\sqrt{\Omega_0 B/2} = \left(\frac{\mu\nu}{0.885}\right)\alpha^2(ZA)^{1/3}\sqrt{\Omega_0 B/2}\,. \tag{32}$$

For large enough Ω_0 the scattering distribution becomes purely Gaussian, since $\eta_{max} \gg 1$ does not hold any longer. In the transition range to this limit the scattering distribution depends perceptibly on the traversed material (see section 2.4.3), since the Gaussian limit is reached earlier for larger ZA.

Although these calculations can be performed much easier within the Molière–Scott formalism applied above, most experimentalists prefer to use for the width of the projected scattering distribution the expression given in ref. [6]:

$$\theta_0 = \frac{14\mathrm{MeV}/c}{p\beta} Q\sqrt{\frac{\Delta x}{X_0}}\left(1 + \tfrac{1}{9}\log_{10}\left(\frac{\Delta x}{X_0}\right)\right). \tag{33}$$

* This is also not treated consistently in ref. [21].

It contains the radiation length X_0, which has basically little to do with multiple scattering. The accuracy of eq. (33) of roughly 10% is due to a fortuitous near-cancellation of complicated Z dependences, and to the logarithmic correction factor introduced by Highland [22], improving the original formula of Rossi [23].

The projected displacements y and z are strongly correlated with their corresponding projected scattering angles θ and ϕ. In the small angle approximation they are Gaussian distributed around the value, which would have occurred for a single deflection by θ at the point $\Delta x/2$ and described by the probability density

$$p(y)\,\mathrm{d}y = \frac{1}{\sqrt{\pi/6}\,\theta_0\,\Delta x}\exp\left[-\frac{(y-\theta\,\Delta x/2)^2}{\frac{2}{3}(\theta_0\,\Delta x/2)^2}\right]\mathrm{d}y. \tag{34}$$

2.2. The GHEISHA simulation of energy loss

The energy loss of charged particles other than e^+ and e^- is simulated in GHEISHA 6/7 in the following way.

The particles are tracked in steps through the detector. The step size is chosen, depending on the mean free path length X_1 for inelastic interactions of nucleons in the medium, to be

$$\Delta x = \begin{cases} \beta^2\dfrac{X_1}{20} & \text{for} \quad \beta^2 \geq 0.01, \\ 0.01\dfrac{X_1}{20} & \text{for} \quad \beta^2 < 0.01, \end{cases} \tag{35}$$

however, without the factor β^2 for gases, and with a few exceptions for unstable particles. The step size is further reduced in those cases where the step would pass a boundary of a detector cell. For each step an average energy loss ΔE is calculated using the formula

$$\frac{\Delta E}{\Delta x} = D\frac{Q^2}{\beta^2}\left[\ln\left(\frac{2m_e c^2 T_e^{\max}}{I^2}\beta^2\gamma^2\right) - 2\beta^2 - 2\delta\right], \tag{36}$$

with $T_e^{\max}$ taken from eq. (5). This expression is similar to formula (1), however, there is a factor of 2 in front of δ, and use is made of an approximation for $T_e^{\max}$ which is not valid for highly relativistic particles. To obtain a numerical value for the mean ionization potential I, approximation (19) is used. The density effect parameters are taken from their general expression (section 2.1.5).

The smearing of the energy loss ΔE is done by the

default version of GHEISHA 7 using a Landau distribution of fixed shape

$$p(\Delta E + 0.31\sigma\Lambda)\,\mathrm{d}\Lambda = \frac{0.762}{\sqrt{2\pi}}\exp\left[-\tfrac{1}{2}(\Lambda^{\alpha} + \mathrm{e}^{-\Lambda})\right]\mathrm{d}\Lambda, \quad (37)$$

with $\alpha = 1$ (0.85) for $\Lambda < 0$ (> 0), whereas default GHEISHA 6 uses Gaussian fluctuations

$$p(\Delta E + \sigma\Lambda)\,\mathrm{d}\Lambda = \frac{1}{\sqrt{2\pi}}\exp\left[-\tfrac{1}{2}\Lambda^2\right]\mathrm{d}\Lambda \quad (38)$$

for all materials, except gases and scintillators. In both cases the width parameter σ is given by

$$\frac{\sigma}{\Delta E} = \frac{2}{\ln(1 + D\,\Delta x/7.5\ \mathrm{eV})}. \quad (39)$$

Since the way in which GHEISHA simulates Landau smearing generates a mean smeared $(\Delta E)_{\mathrm{mean}} = \Delta E + 0.66\sigma$, systematically higher than the initial ΔE from eq. (36), GHEISHA 7 tries to avoid this incorrectness by multiplying the smeared ΔE with a fixed correction factor PARMAT(material,1) for each material. Its default value ranges from 0.86 to 1.00 for solids, from 0.92 to 0.98 for liquids, and from 0.33 to 0.68 for gases.

Optionally, Gaussian fluctuations may be selected by the user setting PARMAT(material,1) to a negative value. In this case PARMAT(material,1) acts only as a flag and no further correction is applied for the smeared ΔE.

In addition to the smeared energy loss, δ-rays are optionally produced in each step. Default GHEISHA 7 generates δ-rays only for muons, and only in gases and liquids, whereas no δ-rays are produced in solids. The user may switch the generation of δ-rays on or off via PARMAT(material,3). Default GHEISHA 6 generates no δ-rays at all, but in drift chamber gas. The production rate of δ-rays in GHEISHA is described by

$$\frac{\mathrm{d}^2 N_{\mathrm{e}}}{\mathrm{d}x\,\mathrm{d}T_{\mathrm{e}}} = D\frac{Q^2}{\beta^2}\frac{1}{T_{\mathrm{e}}^2} \quad \text{for} \quad T_{\mathrm{e}} \le T_{\mathrm{e}}^{\max} \quad (40)$$

which misses the factor $(1 - \beta^2 T_{\mathrm{e}}/T_{\mathrm{e}}^{\max})$ compared to eq. (7). Eq. (5) is again applied for $T_{\mathrm{e}}^{\max}$. The ejection angle is taken from the nonrelativistic formula (6). The δ-ray threshold energy T_{e}^0 is calculated from the default δ-ray range requirement of 1 cm. It can be changed by the user via PARMAT(material,4).

Multiple scattering is simulated in the Gaussian approximation of eq. (27). The width is taken from eq. (33) with a slightly modified parameter value of 15 MeV/c. After each step a displacement is calculated according to

$$y = \frac{\theta\,\Delta x}{2}, \quad (41)$$

which neglects the Gaussian smearing around this value with a width of $\theta_0\,\Delta x/2\sqrt{3}$ (see eq. (34)).

2.3. Muon samples for testing the energy loss simulation

The various features of the GHEISHA simulation of the energy loss of charged particles have been tested with the help of two muon data samples from a non-magnetic calorimeter, the Crystal Ball. The Crystal Ball detector is a highly segmented spherical shell of NaI(Tl) crystals covering 93% of the solid angle. Each crystal, of truncated pyramidal shape, is 40.6 cm deep, corresponding to 15.7 radiation lengths and about one nuclear interaction length. The detector is described in more detail elsewhere [24].

Two $\mu^+\mu^-$ event samples with different muon energies were used. The high energy μ-pair sample comes from the annihilation process $e^+e^- \to \mu^+\mu^-$ at beam energies around 5 GeV. The low energy sample consists of μ-pairs produced in the two-photon reaction $e^+e^- \to e^+e^-\mu^+\mu^-$ where the final state electrons escape the detector under small angles. Here the muon energy typically lies in the range from 200 to 500 MeV. The selection criteria were designed to give unbiased distributions of the muon energy depositions in the calorimeter [25]. The low energy muons were separated from the high energy muons by the requirement not to reach the TOF counters outside the ball, located in a distance of typically 3 m from the interaction point.

2.3.1. Monte Carlo event generation

In order to simulate the two μ-pair samples with Monte Carlo methods, we composed the high-energy sample from the Monte Carlo generator $ee \to \mu\mu(\gamma)$ [26] together with the highest energetic μ-pairs from the Monte Carlo generator $ee \to ee\mu\mu$ [27] according to the corresponding cross sections. Likewise, the low energy Monte Carlo sample was composed from $ee \to ee\mu\mu$ and $ee \to ee\pi\pi$ [28] events. These two samples were subjected to the Crystal Ball detector simulation, the data reconstruction, and analyzed with the same cuts as the real data. The requirement of a missing TOF hit was simulated by a cut on the muon kinetic energy after passing them through the ball. After the selection procedure the events from $ee \to ee\mu\mu$ contributed 7% to the high energy muon sample whereas the events $ee \to ee\pi\pi$ amounted to 8% of the low energy sample. All other background was not exceeding 0.5% in both samples.

The detector response to radiative photons and knock-on electrons was simulated with the EGS 3 code, whereas muons and pions were treated with the GHEISHA 6/7 simulation.

2.3.2. The energy loss distribution of the muons

Having two muon samples with low and high energy muons, respectively, we are able to determine the relativistic rise of the energy loss peak positions between the two samples. The high energy sample contains

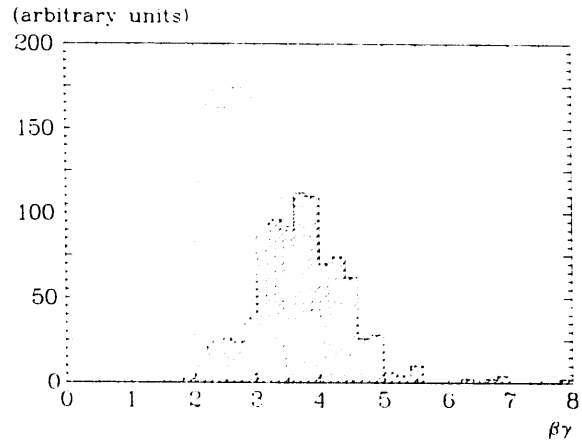

Fig. 1. Monte Carlo prediction of the momentum distribution for the Crystal Ball low-energy muon sample. The hatched part describes the muons which traverse the ball, the other muons range out in the calorimeter.

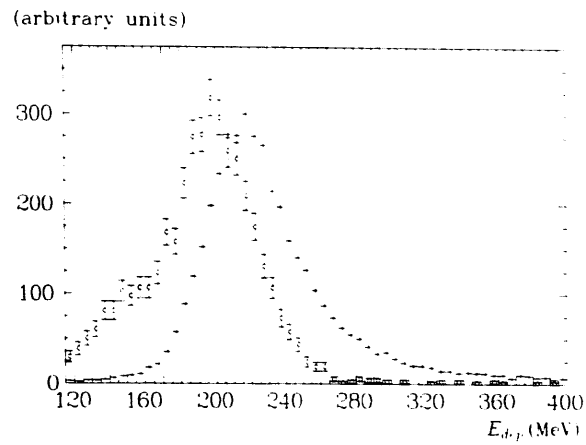

Fig. 3. Energy deposited in the Crystal Ball. The open circles show the low energy muon sample, the crosses the high energy muon sample.

monoenergetic muons with $\beta\gamma = 45$, whereas the low energy muons, according to the Monte Carlo prediction (dashed line of fig. 1), are distributed essentially between $\beta\gamma = 2$ and $\beta\gamma = 5$.

The theoretical prediction for the energy loss peak position $(\Delta E)_{peak}$ of muons in the Crystal Ball, as shown in fig. 2, reveals three momentum ranges, which have to be described by different expressions. Each of them has a counterpart in the Crystal Ball muon samples, as will be seen from the measured distributions of the deposited energy E_{dep}, displayed in fig. 3. The deposited energy E_{dep} of a particle is defined as the sum of the energies over a symmetric group of 13 neighboring crystals including the local maximum at its center. Here all energies are taken into account, which lie well

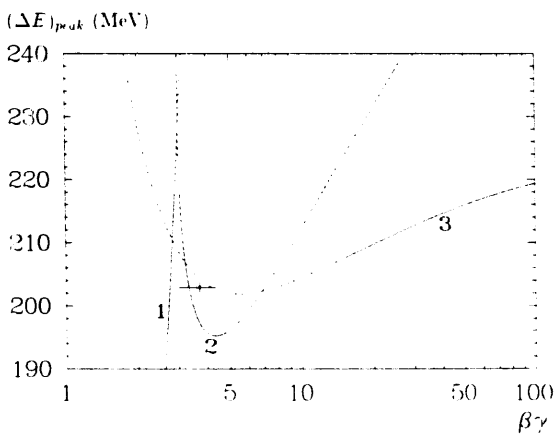

Fig. 2. Prediction for energy loss peak positions of muons in the Crystal Ball. The three curves show the kinetic energy (1), the integrated mean energy loss (2), and the most probable energy loss in thin layers (3). The solid parts indicate the momentum range, where the curves are relevant for the energy loss peak position. The dots are the observed peak values of E_{dep} and their statistical errors.

above the ADC pedestal, resulting in a cutoff at about 0.35 MeV.

– The muons with $\beta\gamma \lesssim 3$ stop in the ball and deposit all their kinetic energy T, so that

$$(\Delta E)_{peak} = T = mc^2\left(\sqrt{\beta^2\gamma^2 + 1} - 1\right) \qquad (42)$$

for any given value of $\beta\gamma$, as depicted in curve no. 1. (Only 13% of the stopping μ^+ decay within the 300 ns time gate of Crystal Ball data taking, and thus deposit more than their kinetic energy *.)

The open part of the histogram in fig. 1 shows the momentum distribution of the stopping muons in the Crystal Ball low energy muon sample, obtained from the Monte Carlo simulation. This part of the low energy muons creates the broad distribution below the Gaussian peak in fig. 3.

– The Gaussian peak in the deposited energy distribution of the low energy sample arises from the more energetic muons, which manage to traverse the ball but do not reach the TOF counters. Their momenta are predicted to be essentially Gaussian-like distributed around $\beta\gamma = 3.5$, as indicated by the hatched part of the histogram in fig. 1.

Their energy loss peak position cannot be described by $(\Delta E)_{mp}$ from eq. (11), since for those low muon momenta the Crystal Ball NaI crystals ($\Delta x = 40.6$ cm, $D_{NaI} = 0.241$ MeV/cm) do not fulfill the conditions to be a thin material layer:

$$\frac{\xi}{T_e^{max}}(\beta\gamma = 3.5) = \frac{11\ \text{MeV}}{12\ \text{MeV}} \approx 1$$

* The GHEISHA simulation of stopped μ^- has been slightly modified by the authors to account for the reduction of their decay probability due to possible capture in atoms.

and

$$\frac{\Delta E}{T}(\beta\gamma = 3.5) = \frac{200\ \text{MeV}}{280\ \text{MeV}} \approx 1.$$

For muons with $3 \lesssim \beta\gamma \lesssim 5$ rather a Gaussian approximation * for the energy loss distribution is appropriate in the Crystal Ball. Then the peak position of the energy loss distribution can be obtained by simply integrating the mean energy loss from eq. (1):

$$(\Delta E)_{\text{peak}} = \int_{0\ \text{cm}}^{40.6\ \text{cm}} \left(\frac{\mathrm{d}E}{\mathrm{d}x}(x)\right)_{\text{mean}} \mathrm{d}x. \tag{43}$$

Using the density effect parameters from material fits [15] yields curve no. 2.

– For the high energy muon sample, however, the Crystal Ball fulfills the conditions of being a thin layer:

$$\frac{\xi}{T_e^{\max}}(\beta\gamma = 45) = \frac{10\ \text{MeV}}{1.4\ \text{GeV}} = 0.007 < 0.05$$

and

$$\frac{\Delta E}{T}(\beta\gamma = 45) = \frac{0.2\ \text{GeV}}{4.7\ \text{GeV}} \ll 1.$$

Thus the peak position in given by formula (11) for the most probable energy loss in thin layers

$$(\Delta E)_{\text{peak}} = (\Delta E)_{\text{mp}}. \tag{44}$$

The result is valid in the Crystal Ball for $\beta\gamma \gtrsim 15$, and yields curve no. 3, again using [15] for the density effect parameters. In the intermediate range $5 \lesssim \beta\gamma \lesssim 15$ none of our formulae is accurate.

The observed peak values lie at $E_{\text{dep}} = 202.9 \pm 1.0$ MeV for those of the low energy muons, which traverse the ball, and at $E_{\text{dep}} = 217.2 \pm 0.4$ MeV for the high energy muons. Since E_{dep} includes the final state photon radiation, an increase in Δx due to the finite vertex distribution, and the detector calibration, which alone may give rise to systematic errors of a few percent, their agreement with the predictions is perfect.

The essential quantity to test a detector Monte Carlo, however, is the difference between the peak positions, since most systematic errors mentioned above cancel in the subtraction. The sensitivity of this test can be seen from the fact, that not only the three parts of the energy loss distributions are described by three different expressions, but also that the predicted $(\Delta E)_{\text{peak}}$ of the muons of $\beta\gamma \approx 3.5$ lies on a curve with a steeply falling slope. Therefore small inaccuracies in the detector simulation and its $\mathrm{d}E/\mathrm{d}x$ parametrization, but also in the underlying momentum distribution from the generator for $\mathrm{ee} \to \mathrm{ee}\mu\mu$, can change the simulated peak value appreciably. To reproduce the relativistic rise of only 7% in the energy loss peak position from $\beta\gamma \approx 3.5$ to $\beta\gamma = 45$ correctly, it is crucial to exactly predict differences between $\mathrm{d}E/\mathrm{d}x$ values for different momenta. Thus the use of an accurate expression for the energy loss is important, including a proper choice of the density effect parameters, which govern the momentum dependence of the energy loss in the relativistic range.

* For these momenta the possible δ-ray energies extend only up to $T_e^{\max} \lesssim 2\xi$, and the number of δ-rays above ξ will be only $\Delta N_e(T_e \geq \xi) \lesssim 1/6$ (eq. (13)), and thus hardly add a distinct tail to the distribution.

2.3.3. The lateral energy pattern of the muons

Another useful test of the GHEISHA detector simulation is to compare the measured lateral energy pattern of the muons with those of the Monte Carlo. Besides the event vertex distribution along the beam axis, there are two major reasons why the deposited energy is generally not restricted to one single crystal: multiple scattering and δ-ray production. While multiple scattering is the dominant effect for low-energy muons, the δ-rays govern the lateral pattern distributions for the high energy muons. This makes it more easy to interpret observed differences between the data and the default Monte Carlo predictions.

Fig. 4 shows various measured distributions of pattern fractions for both samples. They represent the probability, that a given fraction of the deposited energy E_{dep} was distributed among 1, 2, or 4 crystals, and are called F_1, F_2, and F_4 pattern fractions, respectively. For the F_1 and F_2 fractions the crystals with the highest energy deposits are used, whereas the 4 crystals include the one with the maximum energy deposit and its three nearest neighbor crystals. A general feature is, that the low energetic muons tend to extend their energy depositions over more crystals, which results in a tail to lower pattern fractions.

2.4. Changes in the GHEISHA code and resulting improvements

In the following we propose changes and corrections to the GHEISHA code, which are motivated by the observed differences between the GHEISHA simulation formulae (section 2.2), and the theoretical expressions (section 2.1). We will validate the corrections by testing the results with the help of our data distributions.

The changes concern the items δ-ray simulation, energy loss $\mathrm{d}E/\mathrm{d}x$ and its fluctuations, and scattering. In order to disentangle the effects of different changes, we will study each item by leaving the simulation of all other items in their final form.

2.4.1. The δ-ray simulation

Our changes in the GHEISHA δ-ray simulation are:

1) Produce δ-rays in solids, too. (GHEISHA 7 generates them in gases and liquids, only.)
2) Subtract the δ-ray energy from the energy of the tracked particle. (This was simply forgotten in GHEISHA 6/7.)
3) Use the correct relativistic formula (3) for T_e^{max}. (GHEISHA 6/7 uses the approximation (5).)
4) Use the more exact δ-ray production rate (7). (In GHEISHA 6/7 the factor $(1 - \beta^2 T_e/T_e^{max})$ is missing in eq. (40).)
5) Use the correct relativistic ejection angle (4). (GHEISHA 6/7 uses the nonrelativistic limit (6).)

All these changes are made in the subroutine DELRAY. The influence of these changes on the lateral energy pattern distributions from fig. 4 is demonstrated in the following way: Integrating these distributions

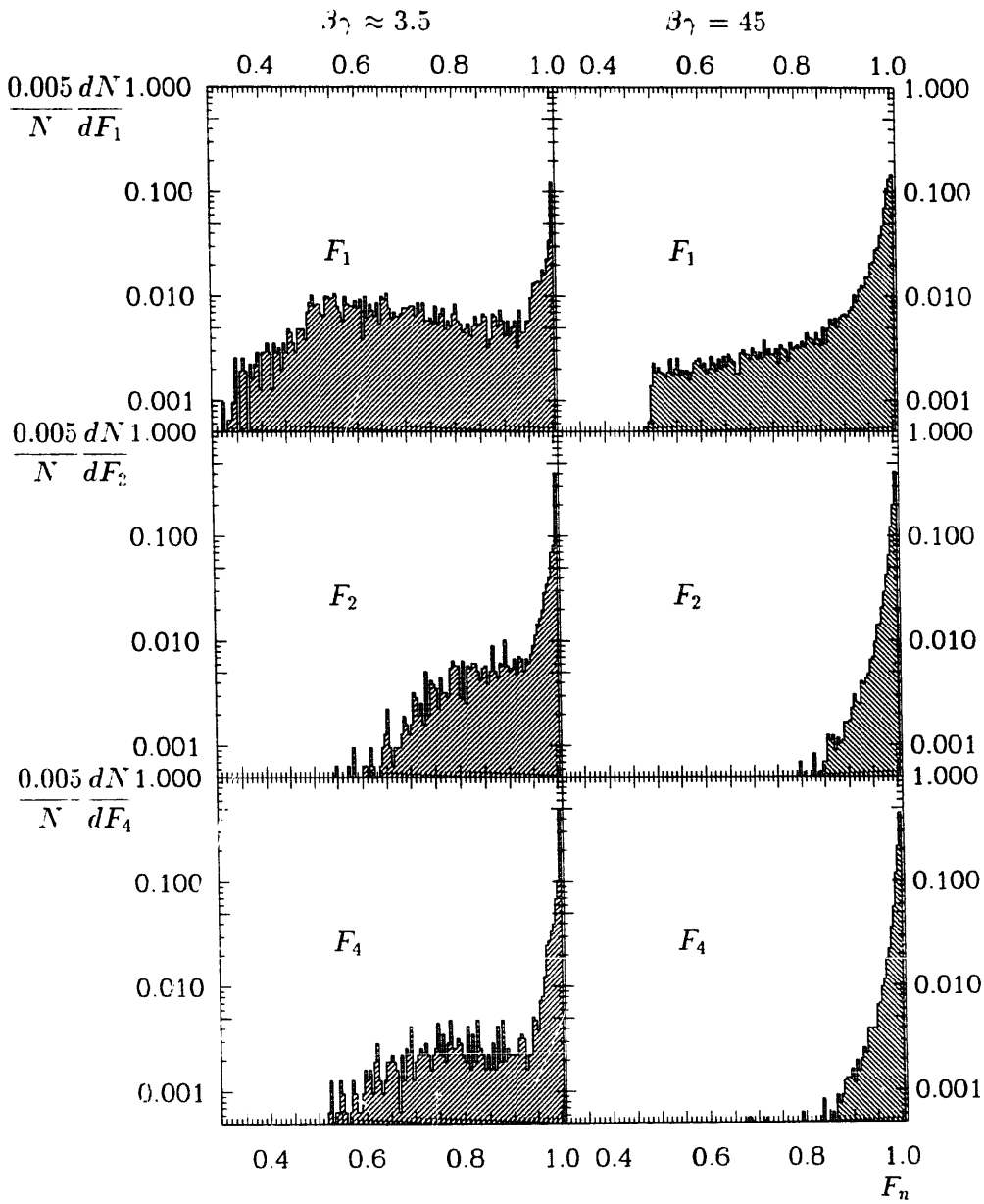

Fig. 4. Distribution of energy pattern fractions as observed with the Crystal Ball detector. The distributions on the left-hand side are obtained from the low energy muon sample, those on the right-hand side come from the high energy muon sample. For the definitions of variables see the text.

from right to left, we get the probability (or cut efficiency) for a muon, having at least a certain fraction of its deposited energy distributed among 1, 2, or 4 crystals (see fig. 5). These efficiencies are compared with the predictions from several Monte Carlo versions.

Change 1). For a finely segmented detector like the Crystal Ball, the lateral energy pattern of charged particles cannot be described without an explicit simulation of δ-rays, since these knock-on electrons may easily extend their electromagnetic showers into the adjacent crystals. This is proven by a large difference in fig. 5 between the integrated pattern fraction distributions of the data (crosses with error bars) compared to the GHEISHA simulation without δ-rays (dotted curve) especially for the high energy muons. The effect on the low energy muons is much smaller, since their T_e^{max} ranges from only 2 to 25 MeV, whereas $T_e^{max}(\beta\gamma = 45) = 1.4$ GeV.

Switching on the GHEISHA δ-ray simulation with a range parameter PARMAT(NaI,4) = 0.6 cm corresponding to a threshold energy of $T_e^0 = 2$ MeV, we obtain the dashed curves in the integrated pattern distri-

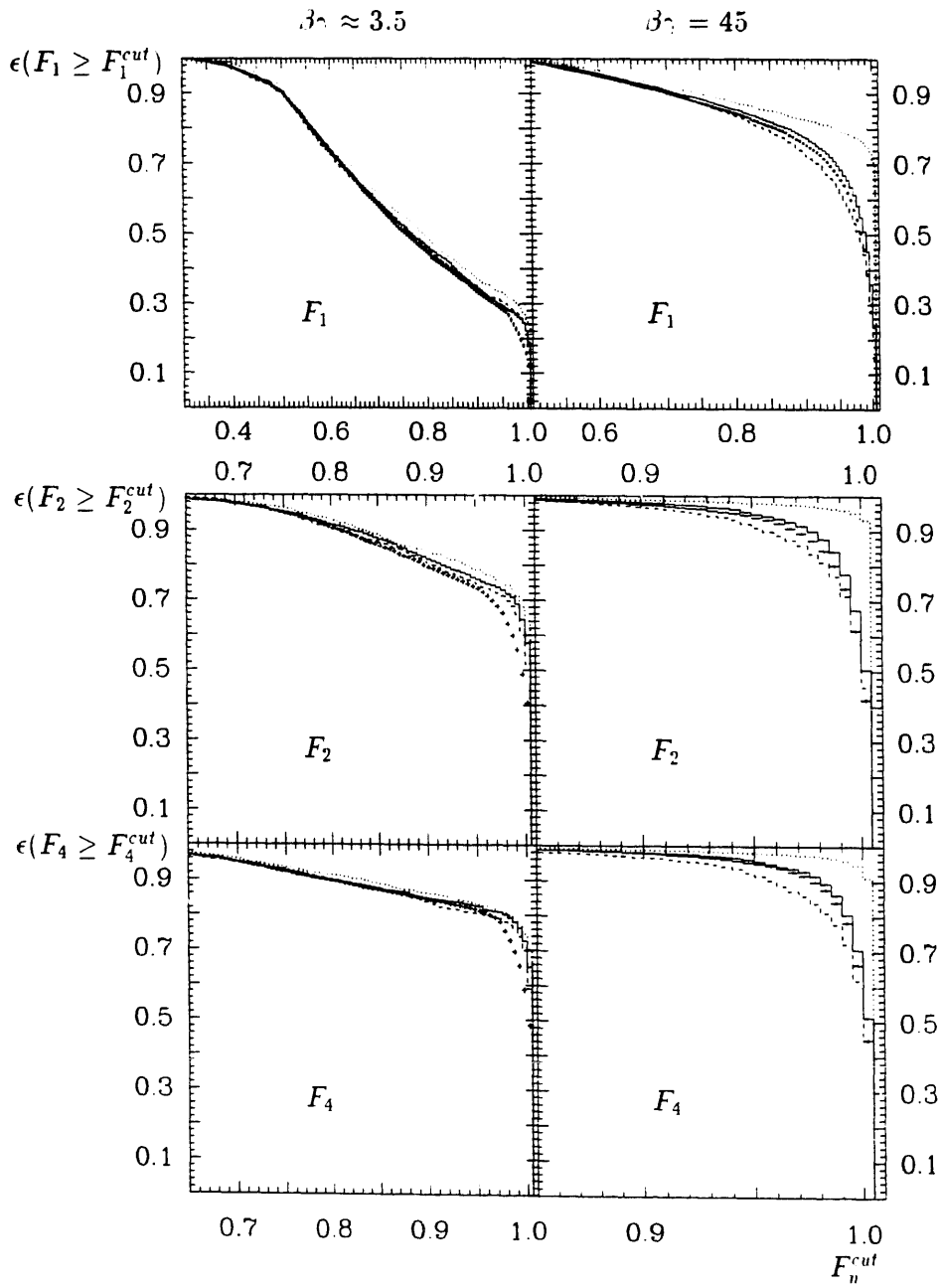

Fig. 5. Efficiency ϵ vs cut on pattern fraction for the low energy muon sample (left-hand side), and the high energy muon sample (right-hand side). Crosses are the Crystal Ball data, solid line is the final Monte Carlo simulation, dots are Monte Carlo without δ-rays, and dashes are Monte Carlo with default GHEISHA δ-rays.

butions. It tends to underestimate the efficiency for the high energy muons by ~ 5% in the most commonly used cut value range below 0.96. Especially the F_4 pattern fractions show a clear difference to the data. This difference will be substantially reduced by our following changes:

Change 2). For the Crystal Ball muon samples this fix does the least change on the lateral pattern as well as on the energy loss, since in general $T_e \ll T$ holds. Only for particles with $T_e^{max} \sim O(T)$, i.e. $\beta\gamma > m/2m_e$ one would expect sizable effects.

Change 3). The correction of the T_e^{max} formula is very small for the low energy muons. Yet, for $\beta\gamma = 45$ it reduces T_e^{max} by 30% from 2.0 to 1.4 GeV. For $\beta\gamma > m/2m_e$, e.g. muons of 11 GeV or more, the GHEISHA formula (5) would even violate energy conservation, since then $T_e^{max} > T$.

For our muon samples, however, this fix plays a vanishing role, since we selected them by requiring the deposited energy of each muon to be less than 400 MeV, restricting the encountered δ-ray energies to values below 200 MeV.

Change 4). The factor $(1 - \beta^2 T_e/T_e^{max})$ has a big influence on the δ-ray production rate near T_e^{max}. While we again are not very sensitive to this region in the high energy muon sample, the simulated δ-rays for the low energy muon sample in fact all lie in the range of $(0.1-1)T_e^{max}$. Thus this modification has a perceptible influence on the pattern fractions simulated for the low energy muons.

Change 5). Of about equal influence for the low energy muons is the use of the correct formula for the δ-ray ejection angle. However, for the high energy muons it causes by far the most important effect on the pattern distributions. This can be seen from fig. 6, where $\cos\theta$ is plotted versus T_e for both the relativistic (4), and the nonrelativistic formula (6) indicated by solid and dashed lines, respectively. For a 20 MeV δ-ray, one finds e.g.

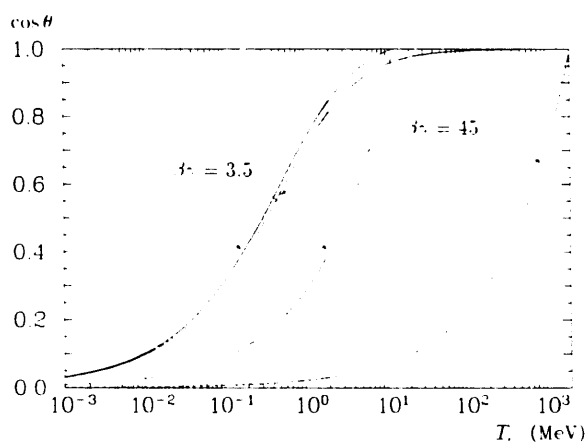

Fig. 6. Theoretical ejection angle for δ-rays. The broken lines result from the nonrelativistic approximation (6), the solid lines show the prediction of the correct relativistic formula (4).

for $\beta\gamma = 45$ almost orthogonal θ values of $\cos\theta = 0.10$ (nonrelativistic), and $\cos\theta = 0.98$ (relativistic).

After applying these five changes to the GHEISHA δ-ray simulation we observe a very good agreement of 1–2% between the integrated pattern fraction distributions of Monte Carlo (solid line in fig. 5) and data (crosses) below 0.96. Only for pattern fraction values near 1 deviations up to 15% for the low energy muons and 5% for the high energy muons still remain. These regions correspond to energy depositions of less than 8 MeV outside the considered crystals, which may be caused by photons radiated off by the final state muons. We estimate, that an appreciable part of the difference for the low energy muons can be explained by this fact, since only the event generator for the high energy muon sample includes final state radiation. A further systematic effect for the low energy sample is introduced by the selection requirement of $F_2 = 1$ for one "tagging muon", which was applied to suppress background from ee → eeee. Exactly at this value the simulated pattern deviates most from the data. Due to the pattern–energy correlation for the "tagging muon" and the energy correlation between the two muons, the energy distributions of the other muon, used for the pattern comparison, may become different for data and Monte Carlo, enhancing already existing differences in the pattern fraction distributions. Finally, an additional systematic error of about 1% for the integrated pattern fractions of the low energy muon sample arises from the uncertainty in the Monte Carlo modeling of the TOF cut. Thus the patterns of the low energy muon sample cannot really test our changes quantitatively on the percent level, but rather show the relative influence.

The remaining differences in the high energy sample may be attributed to inaccuracies in the event generators, in the EGS 3 shower simulation, the ball geometry code, or other error sources.

However, altogether fig. 5 justifies and confirms the correctness of our changes by clearly showing an improvement over the default GHEISHA pattern simulation with and without δ-rays through our corrected δ-ray simulation.

2.4.2. *The energy loss dE/dx and its fluctuations*

Our changes, which affect the energy loss distribution of charged particles are:

1) Explicit and correct simulation of δ-rays (see section 2.4.1, changes 1) to 5));
2) Gaussian fluctuations (38) for the remaining dE/dx (GHEISHA 7 uses Landau fluctuations (37), regardless of whether δ-rays are simulated, or not);
3) Use of the restricted energy loss (9) with T_e^0 as threshold for the δ-ray simulation (GHEISHA uses the mean energy loss (36) with a doubled density effect correction, regardless of whether δ-rays are simulated, or not);

4) A value of the density effect parameter $\bar{C} = 6.06$ [15] for NaI (GHEISHA uses $\bar{C}(\mathrm{NaI}) = 3.40$);
5) Use of the measured mean ionization potentials (table 1) (GHEISHA uses the empirical formula (19));
6) Use of the density effect parameters from material fits (see section 2.1.5) (GHEISHA uses the "general expression").

Changes 1) to 3), and 6) refer to the subroutine DEDX, change 4) is implemented in the material block data, and change 5) in the subroutine MATTER).

We will now study the influence of these changes on the simulation of our two muon samples. For the following comparisons we first adjusted the peak position and width for the energy loss distribution of the high energy sample to match with the data within the statistical errors of 0.3% and 3%, respectively. This was done by applying a dE/dx correction factor of |PARMAT(material,1)| also in case of Gaussian fluctuations (selected by a negative value of PARMAT(material,1) as described in section 2.2), and by introducing a correction factor PARMAT(material,5) for the width in eq. (39). Thus the most probable energy loss of the high energy sample acts as a reference point for the peak position of the Gaussian part of the low energy muon energy loss distribution.

For a correct dE/dx simulation, the factor PARMAT(material,1) should be very close to 1, and deviations, e.g. due to systematic detector calibration errors, should be less than a few percent. Having eliminated this overall systematic erros via PARMAT (material,1), the peak position of the low energy sample can be studied with high enough accuracy to test whether the simulation reproduces the 7% relativistic rise in the energy loss peak position between the two samples.

We study the effect of these changes by means of the generated energy loss distributions in fig. 7. Table 2 lists the corresponding values of peak position and width for the low energy sample, and the correction factors for the high energy sample.

Change 1). Simulating the energy loss in a given detector component, GHEISHA adds up randomly smeared energy losses in a couple of steps. As long as the form of the random fluctuations in the single steps does not depend on the step size, but is fixed as in eq. (37), the result from a sufficiently large number of steps is a Gaussian distribution around the sum of the mean

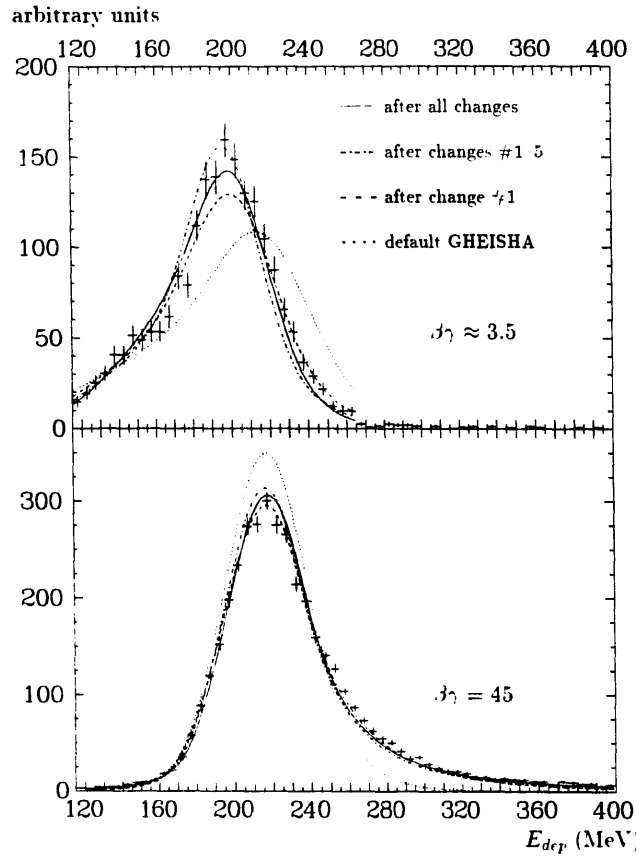

Fig. 7. Simulation of muon energy depositions in the Crystal Ball. The results for the low energy muons are shown in the upper plot, those for the high energy muons in the lower plot. Crosses are data, lines represent Gaussian fits to the results of various versions of Monte Carlo simulation. In the upper plot we added another Gaussian with fixed position for the contribution of the stopping muons, in the lower plot we used power tails to describe the δ-ray contribution on the right-hand side, and the small tail on the left-hand side caused by gaps in the detector. The resulting fit parameters are listed in table 2.

Table 2
Simulation of energy loss peak position and width. The errors given are statistical only

Version (symbol in fig. 7)	$\beta\gamma = 45$		$\beta\gamma \approx 3.5$		
	Peak correction |PARMAT(NaI, 1)|	Width correction PARMAT(NaI, 5)	Peak position [MeV]	Deviation from data [%]	Width [MeV]
Default GHEISHA (dotted)	0.780	3.8	216.9 ± 2.6	+6.9 ± 1.4	23.7 ± 1.5
After change 1) (dashed)	0.745	2.9	201.9 ± 2.0	−0.5 ± 1.1	20.1 ± 1.5
After changes 1–5) (dashed-dotted)	0.975	1.9	196.7 ± 1.3	−3.1 ± 0.8	17.0 ± 1.2
After all changes (solid)	0.995	1.9	201.5 ± 1.8	−0.7 ± 1.0	17.7 ± 1.4
Data values (crosses)			202.9 ± 1.0		17.5 ± 0.8

values of the distributions for the single steps, as follows from the central limit theorem. The dotted curve in the lower plot of fig. 7 shows this behavior for the about 20 steps in the NaI crystals of the Crystal Ball: Even though the single energy losses are smeared according to the Landau fluctuations (37), the summed result appears to be Gaussian and cannot decribe the observed data (crosses). In addition the decrease in the peak position for the $\beta\gamma \approx 3.5$ muons (upper plot of fig. 7) is not observed. Compared to the data the peak position for the low energy muons is thus about 7% too high (see table 2) and the width is incompatibly larger. It is important to note, that this result moreover depends on the chosen simulation step size: The peak position is determined by $(\Delta E)_{\text{mean}}$ in the single steps, which has been shown in section 2.2 to depend on σ and thus on Δx.

Switching on δ-rays explicitly improves the simulation considerably (dashed curves in fig. 7). The high-energy muons are well described with a peak correction factor 0.74, which also reproduces the low-energy muons peak position. Their width deviates by 1.5 s.d. from the data value. This result, however, is based on a purely fortuitous coincidence of several parameters in our given case (see below). It depends on the chosen step size as well as on the δ-ray threshold T_e^0. Since the GHEISHA step size can vary by more than two orders of magnitude for different materials, different particles, or even for the same particle type at different momenta, it is impossible, even including a fixed correction factor PARMAT(material,1), to get a satisfactory description of the energy loss for all particles at all momenta with this simulation. As will be shown, both unwanted dependences are removed by applying our changes 2) to 5).

Change 2). The dependence on the step size Δx can be removed by choosing Gaussian fluctuations for the energy loss below T_e^0. Then the $(\Delta E)_{\text{mean}}$ below T_e^0 does no longer depend on the step size, and the larger energy losses get the proper step size dependence via the δ-ray simulation. In addition the shape of the energy loss in each step is correct, as long as T_e^0 is not much larger than the width σ of the Gaussian. This leads to the rule, to choose for T_e^0 a value close to σ as calculated from eq. (39) for the typical GHEISHA step size Δx in the given material. (e.g. for $\Delta(\text{NaI}) = 2$ cm and $\beta \approx 1$ we choose $T_e^0 \equiv \sigma = 2$ MeV.) However, provided enough computer time is available, one may reduce T_e^0 below this limit in order to simulate δ-ray effects, like the lateral energy pattern, more precisely, or to ensure correct fluctuations even for tiny steps.

Changes 3, 4). Change 3) guarantees the independence of the amount of energy loss from T_e^0. The addition it introduces the theoretically correct formula for dE/dx as a function of the particle momentum. This brings the peak correction factor PARMAT(material,1) to the expected value of about 1 for all materials, given the right material parameters (see changes 4–6) for our case of NaI).

The fact that the default GHEISHA simulation with explicit δ-rays described our two muon samples reasonably well was due to the cancellation of four errors, as can be seen by confronting the theoretically correct formula from eq. (9)

$$\Delta E = D\frac{Q^2}{\beta^2}\Delta x\left[\ln\left(\frac{2m_e c^2 T_e^0}{I^2}\beta^2\gamma^2\right) - \beta^2\left(1 + \frac{T_e^0}{T_e^{\max}}\right) - \delta\right], \tag{45}$$

with the expression (36) used by GHEISHA

$$\Delta E = \text{PARMAT(mat.,1)}\, D\frac{Q^2}{\beta^2}\Delta x \times\left[\ln\left(\frac{2m_e c^2 T_e^{\max}}{I^2}\beta^2\gamma^2\right) - 2\beta^2 - 2\delta\right]. \tag{46}$$

The use of $T_e^{\max} = 2m_e c^2\beta^2\gamma^2$ instead of $T_e^0 = 2$ MeV together with the doubled density correction δ from eq. (13) resulted in a plateau value for high momenta as expected from the correct formula. The resulting error in the amount of the relativistic rise was approximately cancelled by the wrong density effect parameter $\bar{C}$ (change 4)), and the overall amount of dE/dx was corrected by PARMAT(NaI,1). As pointed out above, this approximate cancellation happened just by chance, given our special testing samples, T_e^0 parameter choice, and detector setup.

Change 5). The correction of the mean ionization potential for NaI affects the total amount of dE/dx by about 2% (see section 2.1.5), but has negligible effect on the momentum dependence of dE/dx. Since I and $\bar{C}$ are related via eq. (15), only one of both parameters is needed on the material input file. As GHEISHA already offers $\bar{C}$ on this file, we calculate I from $\bar{C}$ according to

$$I = \hbar\omega_p\, e^{(\bar{C}-1)/2}. \tag{47}$$

The resulting energy loss distributions after changes 1–5) are displayed as dashed–dotted curves in fig. 7. Table 2 shows, that the width of the low energy sample now fits the data well. However, the peak position is too low by about 3%.

Change 6). Our final change is the replacement of the density effect parameters for NaI from the "general expression" (see section 2.1.5) by those from material fits [15], as listed in table 3. Note that the parameters n, Y_0, Y_1, and b are highly correlated, and that even a large variation of these parameters may change the result only marginally. For the Crystal Ball muon samples the modification results in a decrease of the simulated relativistic rise between the two samples from

Table 3
Density effect parameters for NaI

	$\bar{C}$	n	Y_0	Y_1	b
General expression	6.06	3.00	2.86	1.00×10^{3}	1.97×10^{-2}
Material fits	6.06	3.04	1.32	3.91×10^{3}	0.99×10^{-2}

10.4% (20.5 MeV) to 7.8% (15.7 MeV), in good agreement with the observed value of 7.0% (14.3 MeV). The simulated energy loss distributions after all changes are indicated by the solid lines in fig. 7. The size of the decrease is consistent with the expected uncertainty of the "general expression" for the density effect (see section 2.1.5).

The final parameter for the Gaussian width adjustment has the value of 1.9. It accounts for inaccuracies in the amount of the simulated dE/dx fluctuations as well as for the detector resolution of the NaI crystals for ionizing particles. We cannot test the validity of eq. (39) for Gaussian dE/dx fluctuations, since the energy resolution for ionizing particles in the Crystal Ball is not known. That is the reason why we did not separate the detector resolution into the routine MRKRSP, but rather included it in our width correction factor PARMAT(NaI,5) in routine DEDX. For Landau fluctuations of energy losses below T_e^0, applied in the first two Monte Carlo versions listed in table 2, however, is appears impossible to reproduce both widths of the high and low energy sample with a single correction factor.

Altogether the changes 1–6) generate a consistent simulation of dE/dx and its fluctuations, with no additional correction factors dependent on particle, momentum, or material, besides those arising from detector resolution. The simulation describes the energy loss distribution correctly independent of the actual simulation step sizes. This is confirmed by a comparison with our data, which also shows that a proper choice of the density effect parameters is necessary for precise dE/dx simulations.

2.4.3. The simulation of scattering

For the scattering simulation of GHEISHA we propose the following changes of the subroutine SCAT:

1) A smearing of the displacement according to formula (34) (GHEISHA neglects it).
2) Additional simulation of single scattering by combining eqs. (27) and (31) (GHEISHA uses the purely Gaussian approximation (27)).

In order to simulate single scattering, we use for the probability density of the reduced projected scattering angle η a smooth transition of a Gaussian into a $1/\eta^3$ distribution. To model the influence of the finite nuclear size, we assume a sharp cut of the total scattering angle at χ_ν given by eq. (24). For simplicity we divide the complete scattering distribution into a Gaussian part from multiple scattering and an excess over the Gaussian at large reduced angles η, regarded as originated from single scatters. Only the latter part is cut at χ_ν, neglecting possible entries from plural scattering.

The resulting probability distributions of the reduced projected angle are displayed in fig. 8 for the materials

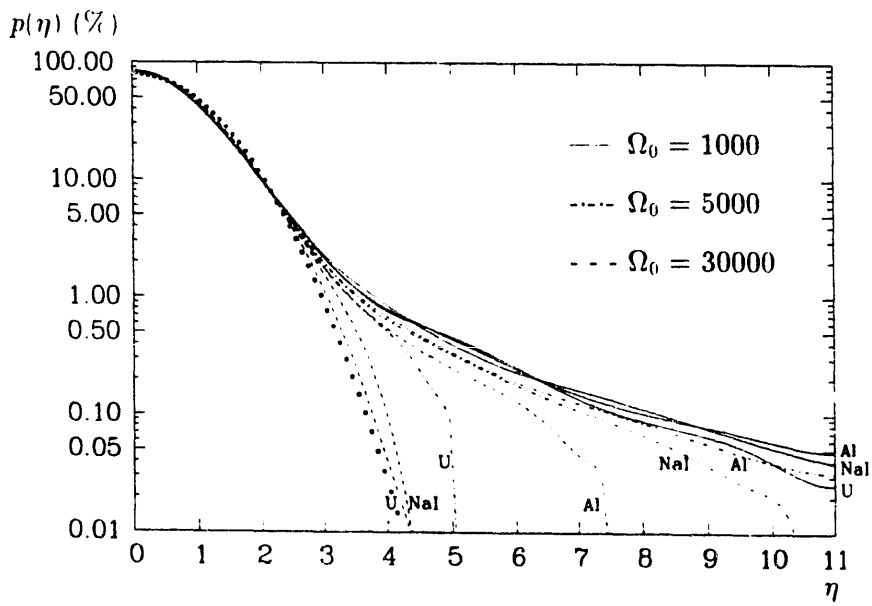

Fig. 8. Probability density of the reduced projected scattering angle. The dots represent a purely Gaussian distribution describing multiple scattering. The lines show the inclusion of single scatters for different Ω_0 values in different materials. The wiggles are due to limited Monte Carlo statistics.

Al, NaI, and U for three different numbers of scatters Ω_0 (compare eq. (26)). The values $\Omega_0 = 1000$, 5000, and 30000 correspond for $\beta \approx 1$ to step sizes of 0.07, 0.35, and 2.1 cm in NaI, respectively. The curves clearly show the dependence on Ω_0 and on the material as expected from the discussion in section 2.1. For $\Omega_0 \lesssim 10^3$ the distributions reveal a pronounced tail of single scatters, independent of the material, but logarithmically increasing with falling Ω_0. For $\Omega_0 \gtrsim 10^5$ an approximately Gaussian distribution will be observed for all three materials.

The GHEISHA choice of Δx (eq. (35)) results in a constant Ω_0 value for solids and fluids independent of the particle and its momentum down to $\beta = 0.1$. The Ω_0 values for the default step sizes range from 15000 for Al, over 30000 for NaI, to 60000 for U. Thus the above study shows that the Gaussian approximation for scattering used by GHEISHA is valid to good accuracy for materials with $Z \gtrsim 30$. For lighter materials, like Al, fig. 8 indicates sizable deviations from this approximation. Only in cases when a cell boundary is crossed and the default step sizes are reduced, which however may frequently happen in finely segmented calorimeters, single scatters may gain influence also for heavier materials.

From this discussion, one expects the influence of the changes in the scattering simulation on the Crystal Ball muon energy pattern to be very small. Indeed, neither the high energy muons are affected, nor are the F_2 and F_4 pattern fractions of the low energy muons. Only in the efficiency simulated for cuts on the F_1 pattern fraction of the low energy sample (see fig. 9) a change of up to 2% is observed.

This effect is just at the border of statistical significance, given the amount of Monte Carlo events. Of course we cannot test the parameters μ and ν in this way, which describe the boundaries of the validity range of the Rutherford formula (20), and influence the relative abundance of single scattering compared to multiple scattering.

3. Simulation of hadronic interactions

The correct simulation of hadronic interactions is of course a even more complex problem than the simulation of energy loss and scattering. The huge variety of hadronic processes covered in GHEISHA, and a lack of precise predictions from theoretical models render in many cases a comprehensive comparison between theory and simulation virtually impossible.

Important information on the ability of the Monte Carlo package to reproduce the detector response to strongly interacting particles, emerges from a comparison with test measurements. They were performed with pion beams (both π^+ and π^-) at CERN using a test setup built of exactly the same NaI(Tl) crystals as the Crystal Ball detector [29]. For further study of hadronic interactions the Crystal Ball detector offers only global event features of multihadron events, like the amount and distribution of deposited energy, since it has no ability of particle identification. The predictions for these event shape variables, however, do not only depend on the detector simulation, but also on the event generator. We used the Lund generator, version 6.2 [30], to model the reactions $e^+e^- \rightarrow$ hadrons and $e^+e^- \rightarrow \Upsilon(1S) \rightarrow$ hadrons.

As will be described in the following, a careful interpretation of discrepancies between these measurements and the Monte Carlo simulation has finally en-

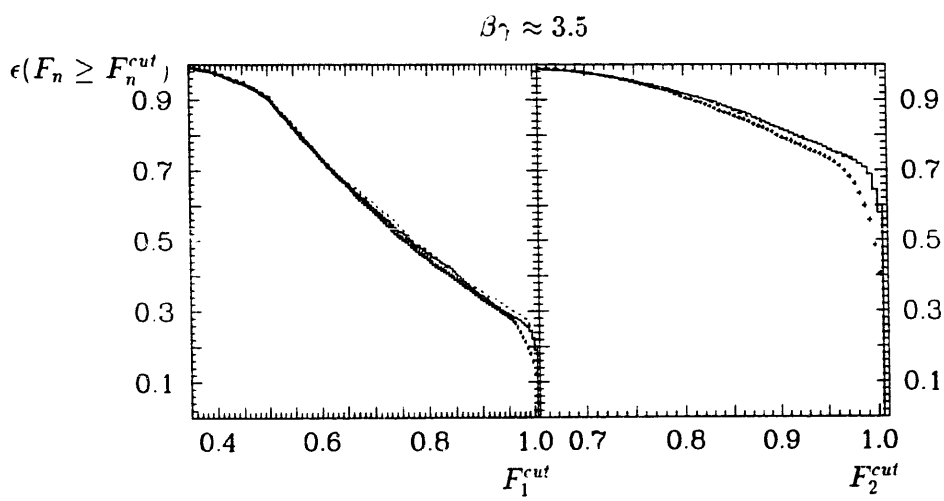

Fig. 9. Influence of scattering on pattern cut efficiency. Crosses represent the data, the solid line the final MC simulation, while for the dashed line no single scattering was simulated.

abled us to find insufficiencies in the GHEISHA simulation of hadronic interactions even without particle identification.

3.1. Comparison of the Crystal Ball data with the Monte Carlo

The multihadron event sample taken by the Crystal Ball group [31] was used to test the simulation of the hadronic interactions of the GHEISHA Monte Carlo [32,33]. Figs. 10–12 show some distributions with striking disagreement between the multihadron data and the standard version of the GHEISHA simulation.

We analyze the event shapes using the momentum tensor $Q^{\alpha\beta}$:

$$Q^{\alpha\beta} = \sum_{i=1}^{N} p_i^2 \delta^{\alpha\beta} - p_i^\alpha p_i^\beta, \qquad \alpha, \beta \in \{x, y, z\}, \qquad (48)$$

where $\boldsymbol{p} = (p^x, p^y, p^z)$ is a pseudo momentum vector formed from the product of the energy deposited in the crystal and the unit vector of the crystal axis. The sum runs over all illuminated ball crystals (N). The smallest eigenvalue obtained by diagonalizing the tensor $Q^{\alpha\beta}$ is denoted by $p^2_{\mathrm{T\text{-}jet}}$. The Monte Carlo prediction for the $p^2_{\mathrm{T\text{-}jet}}$ distribution is shown in fig. 10 together with the one obtained from the hadronic data taken in the continuum at $W = 9.39$ GeV. In addition we display the input distribution without detector response, calculated from the momenta of the generated particles after fragmentation. As can be seen, the measured $p^2_{\mathrm{T\text{-}jet}}$ distribution is governed by apparatus effects.

However, also the p^2_{T} input distribution influences the observed $p^2_{\mathrm{T\text{-}jet}}$, since about two thirds of the hadrons undergo strong interactions in the Crystal Ball calorimeter, and deposit energy correlated to their momenta. In order to obtain agreement with the data we would have to shift the input width σ for the p^2_{T} used in the Lund fragmentation scheme ($2\sigma^2 = \langle p^2_{\mathrm{T}} \rangle$) from 400 to 150 MeV. To get a similar agreement for the Υ(1S) resonance data we would have to make an even more drastic change – to the level of 50 MeV. Such a huge deviation from the default Lund value indicates that there have to be other reasons for the observed discrepancy.

In the Crystal Ball a cluster is defined as a group of geometrically adjacent crystals, each having at least 10 MeV deposited energy. Fig. 11 shows the distribution of the cluster energy of the multihadron events at $W = 9.39$ GeV. The Monte Carlo distribution is shifted towards higher energies with respect to the experimental data.

Taking these two facts together suggests that the energy deposited away from the jet axis is overestimated by the GHEISHA detector simulation. An inspection of the charged particle spectra generated by the fragmentation models of multihadron events reveals a large fraction of particles supposed to range out in the Crystal Ball calorimeter, and gives rise to the expectation, that it is very important to treat stopped particles correctly. For debugging purposes we invented a test Monte Carlo simulation, where negative pions were not allowed to interact strongly after stopping. The fact that the agreement between data and Monte Carlo improved (see fig.

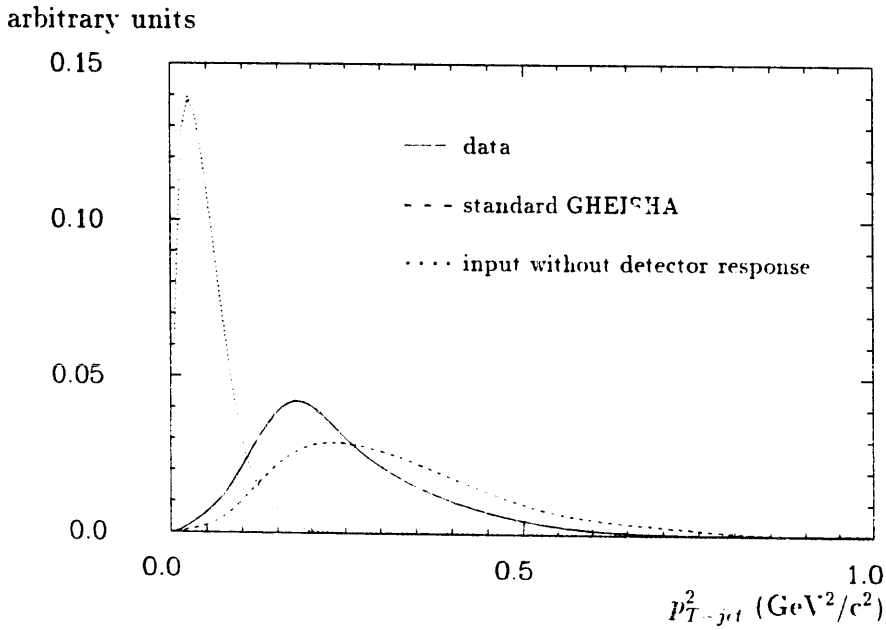

Fig. 10. The $p^2_{\mathrm{T-jet}}$ distribution for the continuum data. The continuous curve shows the Crystal Ball data, the dotted one the input distribution from the generated particles after fragmentation with $\sigma = 400$ MeV, and the dashed line marks the detector response simulation by standard GHEISHA.

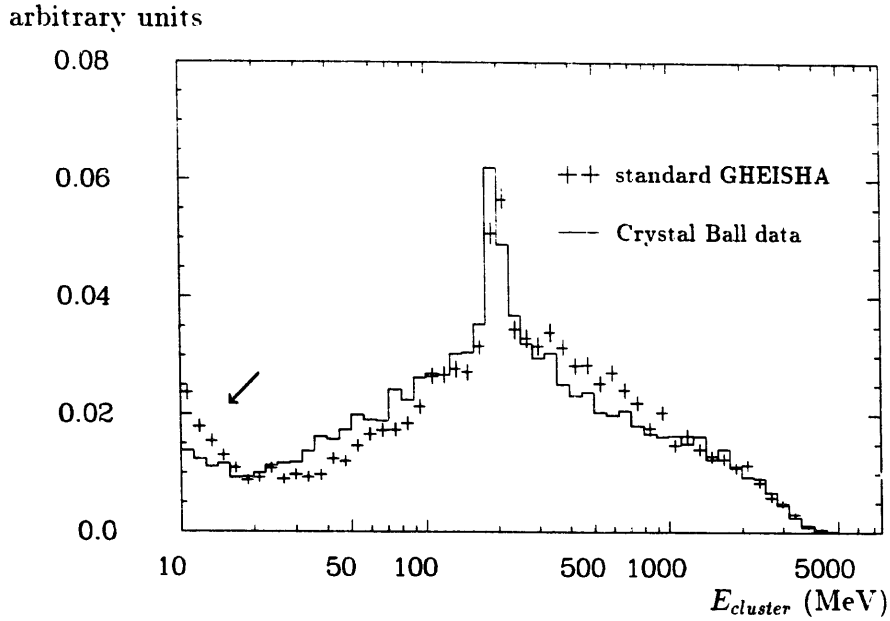

Fig. 11. The distribution of $E_{cluster}$, where each cluster in an event gives an entry. The Crystal Ball data are represented by the histogram. The crosses are the result of the Monte Carlo simulation. The peak at ~ 200 MeV is due to the purely ionizing particles. For the arrow see section 3.2.3.

12), reinforces our expectation. In fact, a close examination of the GHEISHA 6/7 code revealed shortcomings in the treatment of stopped π^- and K^-. Below we will outline the changes which we applied to get a better agreement between data and Monte Carlo.

3.2. Changes of the GHEISHA 6/7 code

Our proposed changes in the GHEISHA code, relevant for the simulation of hadronic interactions, cover the fields of negative particle absorption, light quench-

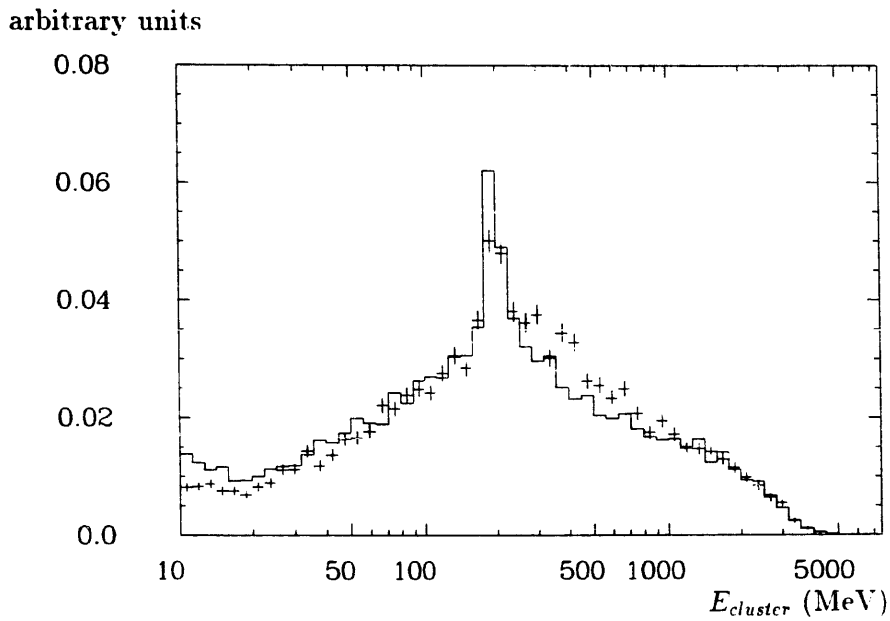

Fig. 12. The distribution of $E_{cluster}$ for a test Monte Carlo simulation, marked by crosses, where negative pions are not allowed to interact strongly after stopping. The histogram represents the same data as in fig. 12.

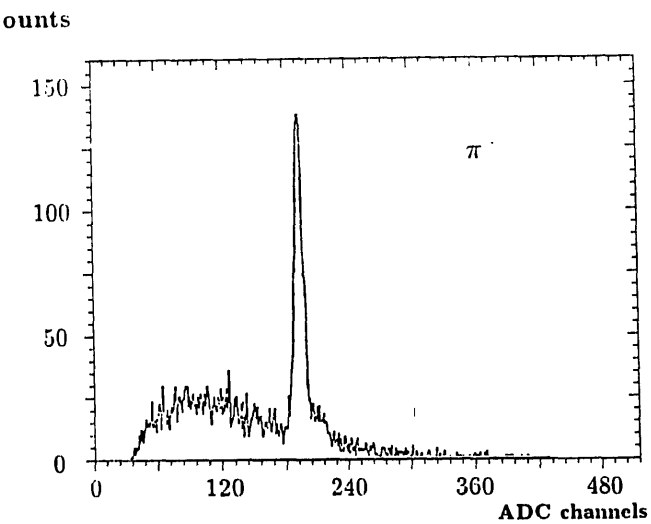

Fig. 13. The pulse height spectrum for 200 MeV/c π^+ in a NaI(Tl) crystal test setup as measured by ref. [29].

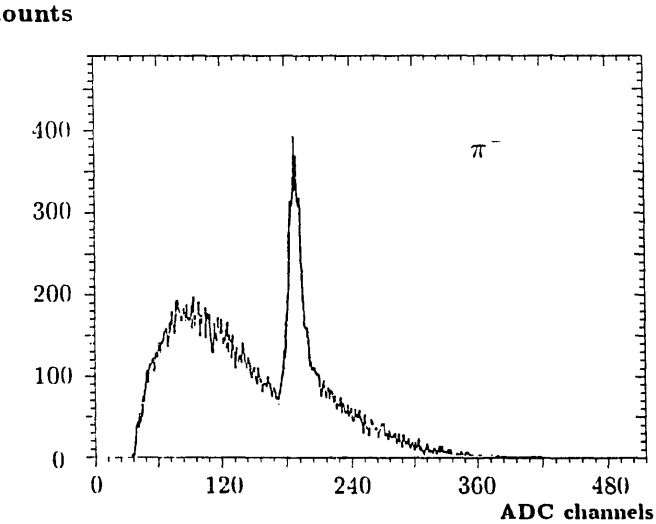

Fig. 14. The pulse height spectrum for 200 MeV/c π^- in a NaI(Tl) crystal test setup as measured by ref. [29].

ing in scintillators, and neutron capture. Of course also the changes described in section 2 are of influence, since all energy depositions in the calorimeter finally proceed via the energy loss of charged particles. In all the following studies we used the final version of the corrected energy loss simulation as described in section 2.

3.2.1. Absorption of negatively charged particles

Positively charged particles stopping in matter simply decay because the Coulomb barrier between the particle and the nucleus prevents nuclear interactions. For slow negatively charged particles (π^-, K^-, Σ^-, etc.) the dominant process is the absorption by nuclei. The Crystal Ball detector response simulation is particularly sensitive to the pion and kaon absorption, as these are the most frequently produced particles. We expect to find on an average about eight charged pions and one charged kaon in a multihadron event at c.m. energies around 10 GeV.

Data from a test setup [29] built of exactly the same NaI crystals as the Crystal Ball detector were used for a comparison with the GHEISHA simulation. The test module was exposed to 200 MeV/c positively and negatively charged pion which stop in the detector. The experimental data of figs. 13 and 14 shows a large disagreement with the GHEISHA simulation (figs. 15 and 16) for negative pions while the positive pions agree reasonably. Although the scales differ (MeV and "ADC channels"), the comparison contains an important message: For π^+ and π^- the measured energy depositions peak at the kinetic energy of the incident particles, whereas the Monte Carlo predicts for stopping π^- mesons a peak at the total energy of the incident particle. This indicates a serious shortcoming in the simulation code. For a proper simulation we need precise experimental data including not only the measurement of the total energy deposition but also of particle multiplicites and energy spectra in π^- absorption processes. Such a measurement was done in connection with a recent cancer therapy study [34] at SIN in Switzerland. The experimental results can be summarized as follows:

1) Only ~75% of the pion mass is available for the kinetic energy of the particles emitted after the absorption process. The rest goes into binding energy.
2) Most of the energy is carried away by neutrons (see table 4).
3) The momentum spectra can be parametrized approximately by an exponential function: ~exp $(-pc/200$ MeV).

An important number is the ratio 5:1 between the number of neutrons and protons. The GHEISHA parametrization assumes this ratio to be ~1:1. Additionally the ratio of protons to heavy fragments was overestimated, and the entire mass of the π^- was assumed to be available for the kinetic energy of the produced particles.

Table 4
Features of particle production in the process of π^- absorption on ^{12}C according to ref. [34]

Particle type	Average multiplicity per π^- stop	Average released kinetic energy per π^- stop [MeV]
n	2.5	76.0
p	0.485	10.4
d	0.356	6.3
t	0.249	3.0
He	0.84	6.2
^{6}Li	0.12	0.8
^{7}Li	0.12	0.8

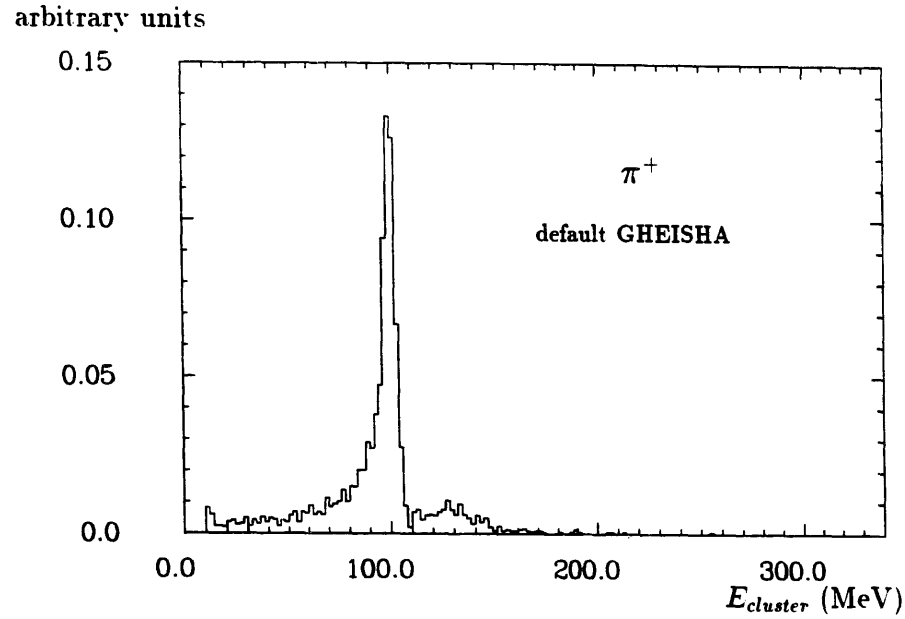

Fig. 15. Default Monte Carlo prediction for the energy distribution of all clusters created by 200 MeV/c π^+ stopping in the Crystal Ball. One pion may give more than one entry.

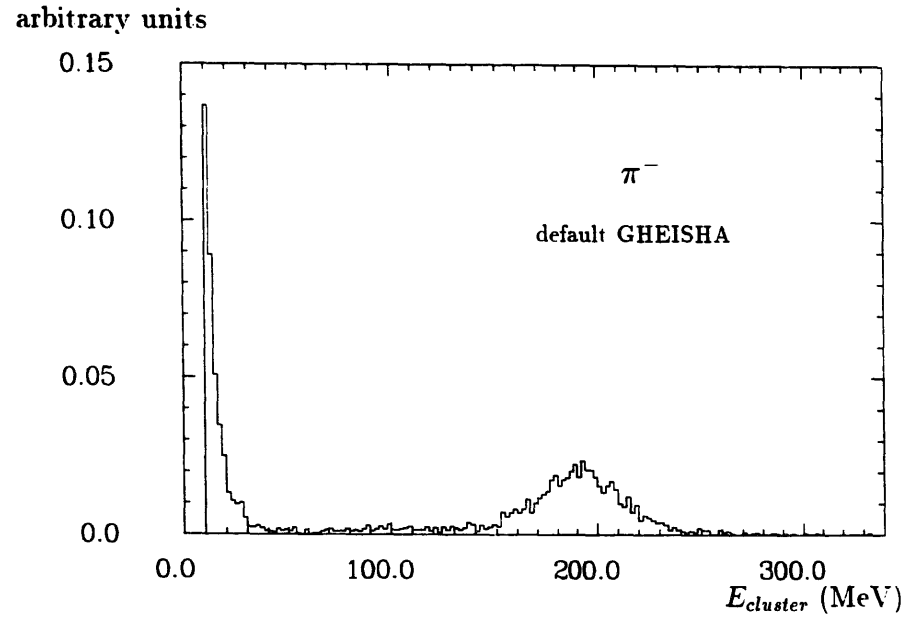

Fig. 16. Default Monte Carlo prediction for the energy distribution of all clusters created by 200 MeV/c π^- stopping in the Crystal Ball. One pion may give more than one entry.

This allows for a qualitative understanding of the discrepancies between our data and the GHEISHA predictions for the $p^2_{\text{T-jet}}$ distributions. Particles with large p^2_{T} usually have lower energy and are stopping. GHEISHA releases a too large fraction of their energy to too many charged secondary particles. This overestimates our measured $\langle p^2_{\text{T-jet}} \rangle$ in the Monte Carlo simulation. The effect is enhanced by the missing simulation of light quenching in NaI (see section 3.2.2 below).

The absorption routine PIMABS was completely rewritten using the measured experimental input. Due to the hermetic structure of the GHEISHA program, allowing for production of fragments heavier than He, is not trivial. We decided to generate all fragments as given in table 4 but afterwards to exclude fragments heavier than He from further tracking. This decision is motivated by the low abundances of the heavy fragments and the observation that the measured energy deposition of heavy fragments will be suppressed by

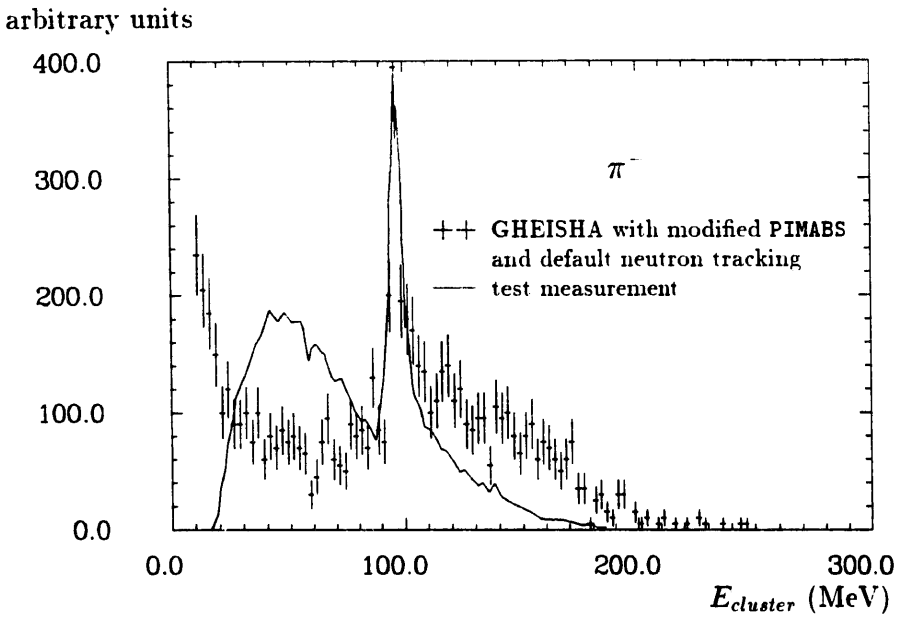

Fig. 17. Comparison of the simulated cluster energy spectrum for stopping π^- (crosses), obtained with the modified absorption routine PIMABS and default neutron tracking, with the measured one from ref. [29] (solid curve).

light quenching in the scintillator. To our knowledge the dependence of the absorption process on the mass of the nucleus was studied neither experimentally nor theoretically. We decided to use directly the results on ^{12}C [34].

The comparison of the visible energy spectrum obtained with the modified π^- absorption routine with the test measurement [29] is shown in fig. 17. The distributions have been normalized to each other to agree in peak height. The energy scale of the test data has been set with the help of the π^+ peak positions. The continuous line shows the shape of the experimental distribution (the same as in fig. 14), while the crosses indicate the results of the simulation. It now gives the peak in the π^- spectrum at the expected position.

However, we still observe clear differences above

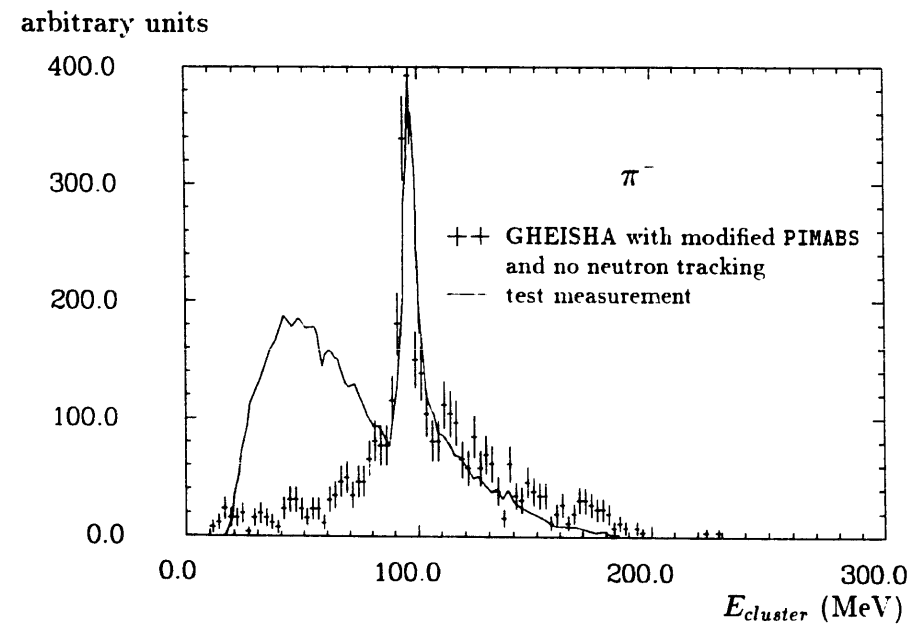

Fig. 18. Comparison of the simulated cluster energy spectrum for stopping π^- (crosses), obtained with the modified absorption routine PIMABS and neutrons excluded from tracking, with the measured one from ref. [29] (solid curve).

and below the peak region. As will be discussed in more detail in section 3.2.3., the simulated range of neutrons is underestimated, and the photons emitted in neutron capture are too energetic in GHEISHA. Thus the neutrons contribute more energy to the π^- clusters than in reality. In addition those neutrons, which leave the π^- cluster region, may create additional low energy clusters when they are captured further away. Those additional clusters clearly show up as a peak at low cluster energies in figs. 16 and 17. As a first test of this assumptions we excluded the neutrons from tracking, which results in fig. 18. Now also the energy depositions above the peak are well described. The broad enhancement below the peak in the measured distribution cannot be explained. It might well be due to beam impurities since muons from the decay of 200 MeV/c pions have a kinetic energy of several 10 MeV.

Similar problems occur in the treatment of stopping K^-. Negative kaons can form hypernuclei or produce other strange particles. The assumption of GHEISHA, to perform only $K^-p \to \Lambda\pi^0$ and $K^-p \to \Lambda\gamma$ in K^- absorption, is again too crude. Table 5 (from ref. [35]) shows the complexity of the processes following negative kaon absorption. We used these probabilities to simulate negative kaon absorption in the routine KMABS, assuming that the absorption process takes place as on free p, n and two-nucleon aggregates (NN). The numbers are normalized such that the branching ratios for K^-p, K^-NN, and K^-n add up to 100% each. The process of K^- absorption on two-nucleon aggregates has a probability rather independent of the target

Table 5
Elementary processes for pion and hyperon production from K^- absorption [35]

	Initial state	Final state	Branching ratio [%]
Production	$K^- + p$	$\Sigma^+ + \pi^-$	22
		$\Sigma^0 + \pi^0$	28
		$\Sigma^- + \pi^+$	44
		$\Lambda + \pi^0$	6
	$K^- + n$	$\Sigma^0 + \pi^-$	30
		$\Sigma^- + \pi^0$	30
		$\Lambda + \pi^-$	40
	$K^- + NN$	$\Sigma^+ + N$	33
		$\Sigma^0 + N$	33
		$\Sigma^- + N$	33
Decay	free Σ^+	$n + \pi^+$	48
		$p + \pi^0$	52
	free Σ^0	$\Lambda + \gamma$	100
	free Σ^-	$n + \pi^-$	60
		absorption	40
	free Λ	$n + \pi^0$	36
		$p + \pi^-$	64

used and contributes about 20% to the total absorption rate for targets heavier than deuterium [35]. The relative probability for the absorption taking place on a single neutron or proton within the nucleus is taken to be equal to the $(A - Z)/Z$ ratio. Formation of hypernuclei was not simulated.

The main result of this treatment is that not only neutral but also charged pions are directly produced in K^- absorption, and that the pion energies now vary from about 170 MeV for the processes involving Λ production to about 500 MeV in those cases where the absorption takes place on two-nucleon aggregates. As an example let us mention that the mean visible energy for 400 MeV/c stopping K^- in the Crystal Ball is reduced from 500 to 380 MeV through our changes, and that the visible energy distribution is broadened.

3.2.2. Light quenching in scintillators

The scintillation efficiency in both organic and impurity-activated inorganic crystals is defined by the fraction of the energy loss dE/dx of the incident particle, which is emitted as scintillation light dL/dx. However, the theory of the scintillation process is different for both cases [36]. In organic crystals the scintillation arises from the transition of excited molecules into the ground state. Their excitation may have proceeded either directly by the incident particle or via energy transfer from other excited molecules (sometimes described as "exciton" diffusion). In inorganic crystals the light is emitted exclusively from the impurity sites after an excitation by exciton capture. The excitons are generated by the energy loss in the crystal lattice. Direct excitation of the activator centres is in general negligible.

If the rate of energy dissipation processes competing with scintillation depends on the primary dE/dx, the scintillation efficiency will not be constant, and the scintillation response $dL(dE)$ becomes nonlinear. For both organic and inorganic scintillators the semiempirical formula [36]

$$\frac{dL}{dx} \propto f \frac{dE/dx}{1 + \epsilon\, dE/dx} \tag{49}$$

describes the measured data with the help of a quenching parameter ϵ.

The factor f in (49) is relevant only for inorganic crystals resulting in a threshold behavior of the scintillation efficiency at small dE/dx:

$$f = \begin{cases} 1 & \text{for organic scintillators,} \\ \dfrac{k\, dE/dx}{1 + k\, dE/dx} & \text{for inorganic scintillators.} \end{cases} \tag{50}$$

It gives the number of excitons per electron–hole pair created by the incident particle [37]. Its deviation from one comes from electron trapping at lattice defects and is described by the parameter k.

The second factor in (49) can be motivated for organic as well as for inorganic scintillators by assuming two types of energy dissipation processes other than scintillation: The first type having a rate independent of dE/dx (e.g. internal conversion to molecular vibration energy for organics, crystal defects acting as traps for the excitons for inorganics), and the rate of the second type linearly depending on dE/dx. The existence of the latter type of processes gives rise to light quenching. Following ref. [38], the scintillation response can then be obtained from an ansatz neglecting "exciton" diffusion to be

$$\frac{dL}{dx} \propto \frac{\ln(1 + 2\epsilon\, dE/dx)}{2\epsilon}, \tag{51}$$

which can be expanded yielding the second factor of (49) for sufficiently small dE/dx.

For organics, a detailed model for the second type of energy dissipation processes [39] yields even directly the second factor of formula (49). It includes quenching of an excited molecule through interaction with neighboring excited molecules, diffusion of the so-called "excitons" and quenching of such an "exciton" at damaged or ionized molecules along the particle path.

For inorganic crystals a proposed model [37], motivating the second factor of (49) from a saturation of the activator centers, has been rules out [40]. Instead the results indicate the quenching of excitons by the crystal lattice, independent of the concentration of the impurity centers, but dependent on the primary dE/dx. A theoretical model for this is missing, however.

The standard GHEISHA code accounts for light quenching only for plastic scintillator. The only way light quenching can be achieved for other materials is an explicit change in the GHEISHA subroutine MRKRSP enabling the call to LGTSAT. GHEISHA parametrizes the effect of light quenching by

$$\frac{\Delta E_{\text{seen}}}{\Delta x} = \frac{\frac{\Delta E}{\Delta x}}{1 + \epsilon \frac{\Delta E}{\Delta x}}, \tag{52}$$

where ΔE_{seen} is the observed energy deposition including the detector calibration, ΔE is the calculated energy loss, and ϵ is the quenching parameter. For particles with charge Q greater than unity ϵ is modified to

$$\tilde{\epsilon} = 0.8\epsilon Q. \tag{53}$$

In the absence of a theory for inorganic crystals we decided to return to the material independent motivation (51) of light quenching and use for NaI:

$$\frac{\Delta E_{\text{seen}}}{\Delta x} = \frac{\ln\left(1 + 2\epsilon \frac{\Delta E}{\Delta x}\right)}{2\epsilon}. \tag{54}$$

Fig. 19 shows that this parametrization, compared to eq. (52), results in a slightly smaller light quenching (i.e. increases the ratio $\Delta E_{\text{seen}}/\Delta E$) at large values of $\epsilon \Delta E/\Delta x$. Furthermore a saturation of $\Delta E_{\text{seen}}/\Delta x$, like in eq. (52), does not occur. The quenching parameter was scaled by density from BGO, assuming $\epsilon\rho$ to be a material independent constant for inorganic scintillators

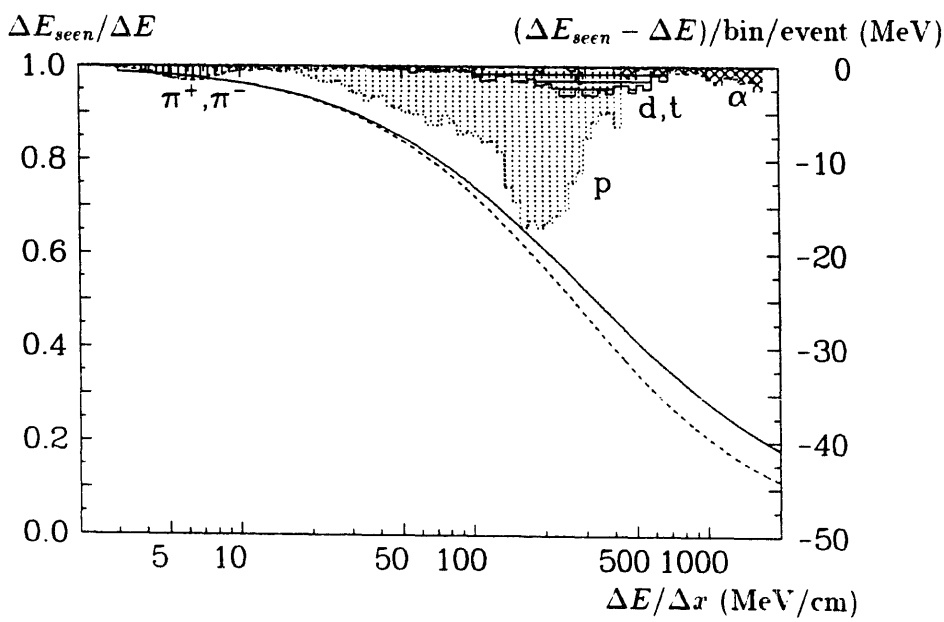

Fig. 19. The influence of light quenching. The dashed line is the GHEISHA parametrization (52), the full line shows the result from formula (54) calculated with the same quenching parameter. Both lines refer to the left-hand scale. The shaded areas show the dark energy per bin due to light quenching for different particle types in a typical multihadron event for the Crystal Ball detector; here the right-hand scale applies.

[1], and yielding $\epsilon(\mathrm{NaI}) = 0.0038$ cm/MeV. The choice of ϵ is highly uncertain, since it depends on the purity and the radiation damage of the crystals. The factor f in (49) was set to 1, neglecting threshold effects in the scintillation efficiency (see below).

Applying our parametrization, light quenching is non-negligible for the simulation of hadronic interactions. Fig. 19 shows the average dark energy due to light quenching for different particle types (including all secondary particles) in a typical multihadron event in the Crystal Ball detector at c.m. energies around 10 GeV. In total about 400 MeV/event cannot be detected, out of which ~ 300 MeV are from protons. This has to be compared to a typical visible energy of 5000 MeV for hadronic events.

Because we are using the energy deposits from the crystals to define the $p^2_{\mathrm{T\text{-}jet}}$ variable, quenching changes the $p^2_{\mathrm{T\text{-}jet}}$ distribution dramatically, as it lowers the observed "off jet-axis" energy deposits emerging mainly from the nuclear interactions in the calorimeter. The energy deposited "on jet-axis" is much less affected by the light quenching effect because the particles produced close to the jet-axis are usually energetic. After accounting for light quenching the simulated $p^2_{\mathrm{T\text{-}jet}}$ distribution of multihadron events in the Crystal Ball nicely agrees with the data (see fig. 20).

Let us note, that this effect would have been just inversed, if we used in (eq. 54) the factor f from (49) with a parameter $k\rho(\mathrm{NaI}) = 2$ g/MeV cm^2 [37]. In this case the light output of protons would not have been decreased, but increased with respect to the lower $\mathrm{d}E/\mathrm{d}x$ of electrons, muons, and pions. Thus the data do not support such a low value of $k\rho$ for the NaI crystals of the Crystal Ball.

3.2.3. Neutron transport

As was noticed by various authors [41,42] neutron absorption and transport is extremely difficult to simulate correctly. Compared to neutron energies in the MeV range, the cross section for capture is large for neutron energies of several keV, but very large for energies below the eV level and for thermal neutrons. In our case the energies of secondary produced neutrons are of the order of MeV. The GHEISHA 6 code treats them as thermal as soon as their energies fall below a cutoff value of 1 MeV. In this way we get only a very crude picture of neutron interactions: As they lose their energy slowly – mainly by elastic scattering – neutrons with few MeV can travel far inside the detector before being captured by nuclei. The neutron absorption process can be described as a (n, γ)-reaction where the γ quantum has a well-defined energy typical for the nucleus in which the absorption takes place. GHEISHA 6/7 assumes that the absorption leads to emission of gamma quanta with a total energy of 8 MeV, a typical nucleon binding energy. The energy is emitted in two bursts: one gamma is generated with its energy taken from a Gaussian distribution with a mean of 6.5 MeV and 1 MeV spread, then a second gamma is generated to reach the 8 MeV deexcitation energy. This approximation is only sufficient for applications where high accuracy down to deposited energies of a few MeV is not required. Because of the 10 MeV threshold for the Crystal Ball cluster energy we have to simulate the absorption process with more care, as can be seen in figs. 11 and 12. In fact, the mean energy released in the capture process of neutrons in NaI is much lower than 8 MeV [43]. We have modified the GHEISHA routine CAPTUR so that γ lines with a total energy of about 3

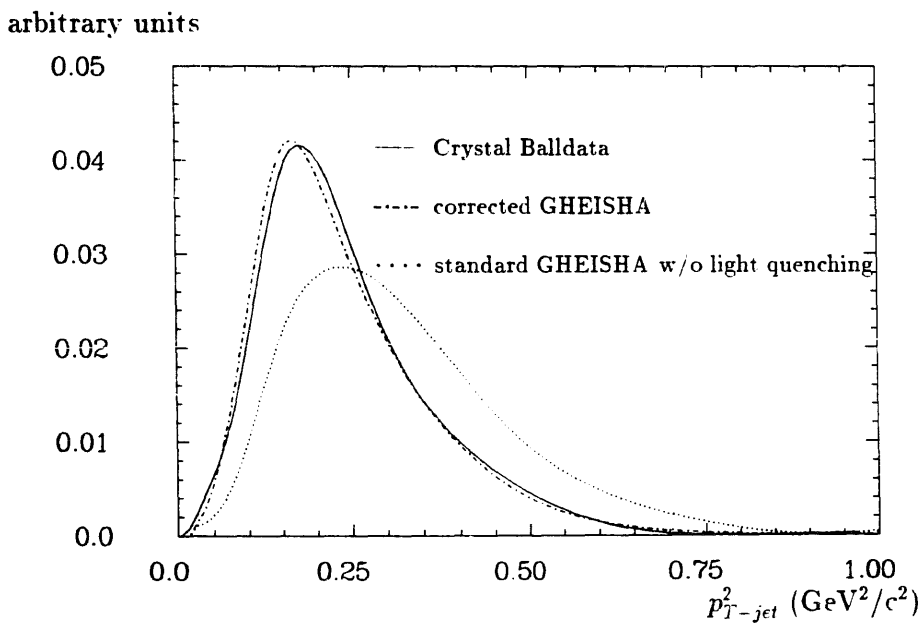

Fig. 20. The $p^2_{\mathrm{T-jet}}$ distribution for the continuum data before accounting for light quenching (dotted) and after all changes (dashed-dotted) compared to the data (solid).

MeV are emitted for NaI, whereas we use the default GHEISHA procedure for the other inactive materials in the Crystal Ball detector. These changes were necessary to describe the data just above the threshold of E_{cluster}, as demonstrated in fig. 21.

The cutoff value for the neutron transport was not changed. An improvement is readily available through the routine NSLDOW in GHEISHA 7, which simulates the moderation down to thermal energies. However, our studies of neutron simulation were done with GHEISHA 6, only.

4. Summary

The increasing accessible and measurable energy range of high energy physics causes that the detector simulation programs grow in size and complexity. This renders the programs very hard to change and to debug. Nonetheless, combining several Monte Carlo testing techniques and comparing the results to experimental and theoretical knowledge, we were able to go beyond the level of simple tests and to propose substantial improvements of the GHEISHA code.

As a by-product of reviewing the well-known theory of energy loss we deduced an expression for the restricted energy loss with an extended range of validity. Important dependences on layer thickness and material re-emerge from our study of the multiple scattering theory suggesting caution in the application of the Gaussian approximation for the finite step sizes used in Monte Carlo calculations.

Our proposed changes in the GHEISHA energy loss routines considerably improve the δ-ray treatment and create a consistent simulation of dE/dx and its fluctuations, expected to work without any ad hoc correction factors regardless of material or simulation step size. In addition we propose to extend the GHEISHA multiple scattering parametrization to account for single scattering.

Concerning the modeling of hadronic interactions, the GHEISHA package covers the large variety of possible processes with an unprecedented completeness. However, further improvements are suggested, which affect the abundance, type, and energy of secondary particles released in the absorption process of negative pions and kaons. It is shown that light quenching in scintillators is an important effect, which cannot be neglected. However, there is a great uncertainty in its parametrization. We encounter difficulties in correctly treating interactions of neutrons. In this context a general problem for the modeling of hadronic showers shows up. In contrast to the electromagnetic case (EGS) the meaning of a simple energy cutoff in terms of the required simulation accuracy becomes unclear, since processes below the cutoff may gain importance.

Concluding, the performance of a detector Monte Carlo depends on the modeling of hadronic showers even down to energies of few MeV as well as on the energy loss simulation which finally converts all processes into measurable signals. Our proposed changes in both fields are motivated from theoretical and experimental reasoning. They are additionally supported by a distinct improvement in the description of the Crystal Ball data, though not always complete agreement with the measurements is obtained. A similar influence can

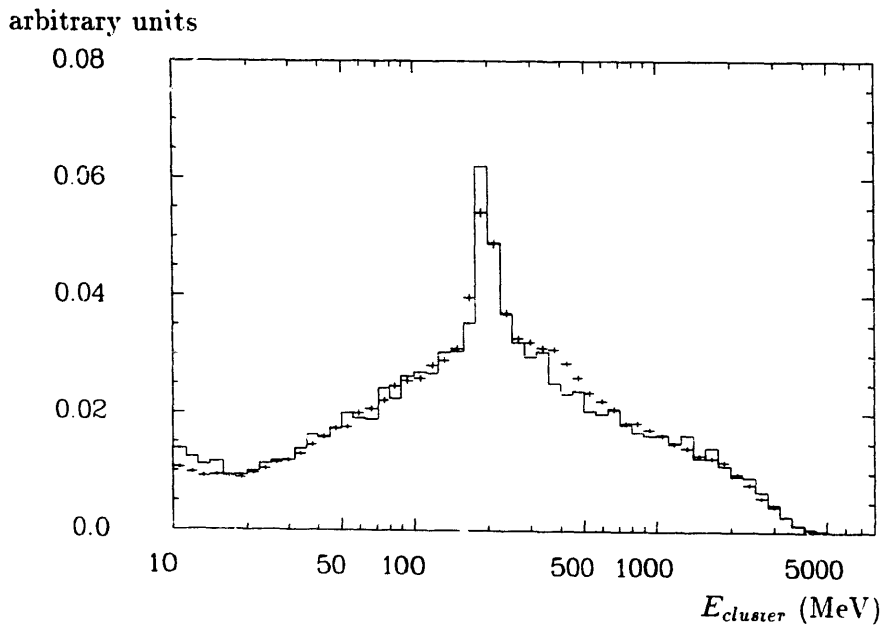

Fig. 21. The distribution of E_{cluster}. The data are represented by the histogram. The crosses are the result of the final Monte Carlo simulation.

be expected on the GHEISHA simulation of the detector response also for other calorimetric detectors or high precision energy loss measurements.

Finally, we would like to mention that most changes concerning energy loss and δ-rays have already been implemented by H. Fesefeldt in the latest update of GHEISHA, version 8. Those changes, however, have no effect on GHEISHA in GEANT, since GEANT has its own energy loss simulation.

Acknowledgements

This study was very much inspired by our work within the Crystal Ball collaboration. We are indebted to all people of the Crystal Ball collaboration * since we could base the verification of our changes of the GHEISHA program on data from the Crystal Ball. We would especially like to thank J. Dillon, J. Gaiser, S. Keh, S. Leffler, W. Lockman, and C. Rippich who provided the basic framework of the Crystal Ball Monte Carlo code.

We appreciate the support of W. Metzger in creating the hadronic Monte Carlo samples and passing them repeatedly through new versions of the detector simulation.

We thank H. Fesefeldt for valuable discussions. Substantial help to improve the clearness in outline, presentation, and phrasing of this report came from discussions with U. Volland, W. Koch, J.K. Bienlein, H. Wegener, and K. Karch.

We would like to thank the DESY directorate for its hospitality and financial support. M.K. acknowledges financial support from the German Federal Minister for Research and Technology (BMFT) under contract number 054 ER 12P.

* D. Antreasyan, Ch. Bieler, J.K. Bienlein, A. Bizzeti, E.D. Bloom, K. Brockmüller, A. Cartacci, M. Cavalli-Sforza, A. Compagnucci, G. Conforto, S. Cooper, D. Coyne, K. Fairfield, G. Folger, A. Fridman, G. Glaser, G. Godfrey, K. Graaf, F.H. Heimlich, F.H. Heinsius, R. Hofstadter, J. Irion, H. Janssen, Z. Jakubowski, K. Karch, S. Keh, T. Kiel, H. Kilian, I. Kirkbride, M. Kobel, W. Koch, A.C. König, K. Königsmann, S. Krüger, G. Landi, R. Lekebusch, S. Lowe, B. Lurz, H. Marsiske, W. Maschmann, P. McBride, H. Meyer, W.J. Metzger, B. Monteleoni, B. Muryn, B. Niczyporuk, G. Nowak, P.G. Pelfer, M. Reidenbach, M. Scheer, P. Schmitt, J. Schotanus, J. Schütte, D. Sievers, T. Skwarnicki, V. Stock, K. Strauch, U. Strohbusch, J. Tompkins, B. van Uitert, R.T. Van der Walle, A. Voigt, U. Volland, K. Wachs, H. Wegener and D. Williams from the following institutions: California Institute of Technology, Carnegie-Mellon University, Cracow Institute of Nuclear Physics, Deutsches Elektronen Synchrotron DESY, Universität Erlangen-Nürnberg, INFN and University of Firenze, Universität Hamburg, I. Institut für Experimentalphysik, Harvard University, University of Nijmegen and NIKHEF-Nijmegen, University of California at Santa Cruz, Department of Physics, HEPL, Stanford Linear Accelerator Center, Stanford University and Universität Würzburg.

References

[1] H. Fesefeldt, Aachen preprint, PITHA 85/02, and corresponding source code.
[2] H.A. Bethe, Ann. Phys. 5 (1930) 325.
[3] F. Bloch, Z. Phys. 81 (1933) 363.
[4] E.J. Kobetich and R. Katz, Phys. Rev. 170 (1968) 391.
[5] E.A. Uehling, Ann. Rev. Nucl. Part. Sci. 4 (1954) 315.
[6] Particle Data Group, G.P. Yost et al., Phys. Lett. B204 (1988) 1.
[7] L.D. Landau, J. Phys. USSR 8 (1944) 201.
[8] H.D. Maccabee and D.G. Papworth, Phys. Lett. A30 (1969) 241.
[9] W.F.G. Swann, J. Frank. Inst. 226 (1938) 598.
[10] E. Fermi, Phys. Lett. 57 (1940) 485.
[11] R.M. Sternheimer, Phys. Rev. 88 (1952) 851;
R.M. Sternheimer, Phys. Rev. 91 (1953) 256.
[12] R.M. Sternheimer, Phys. Rev. 145 (1966) 247.
[13] R.M. Sternheimer and R.F. Peierls, Phys. Rev. B3 (1971) 3681.
[14] R.M. Sternheimer, Phys. Rev. 93 (1954) 1434;
R.M. Sternheimer, Phys. Rev. 103 (1956) 511;
R.M. Sternheimer, Phys. Rev. 164 (1967) 349;
R.M. Sternheimer, Phys. Rev. B24 (1981) 6288;
R.M. Sternheimer, M.J. Berger and S.M. Seltzer, Phys. Rev. B26 (1982) 6067, erratum Phys. Rev. B27 (1983) 6971.
[15] R.M. Sternheimer, M.J. Berger and S.M. Seltzer, Atom. Data Nucl. Data Tables 30 (1984) 261.
[16] T. Mayer-Kuckuk, Kernphysik (Teubner, Stuttgart, 1979).
[17] B.P. Nigam, M.K. Sundaresan and T.-Y. Wu, Phys. Rev. 115 (1959) 491.
[18] H. Jérémie and B. Lorazo, Nucl. Instr. and Meth. A268 (1988) 281;
M.N. Butler et al., TRIUMF preprint, TRI-PP-89-12 (1989).
[19] G. Molière, Z. Naturforsch. 2a (1947) 133 and 3a (1948) 78.
[20] W.T. Scott, Rev. Mod. Phys. 35 (1963) 231.
[21] J.D. Jackson, Classical Electrodynamics (Wiley, New York, 1975).
[22] V.L. Highland, Nucl. Instr. and Meth. 129 (1975) 497.
[23] B. Rossi and K. Greisen, Rev. Mod. Phys. 13 (1941) 240.
[24] E.D. Bloom, C.W. Peck, Ann. Rev. Nucl. Part. Sci. 33 (1983) 143;
K. Wachs et al., Z. Phys. C42 (1989) 33.
[25] Z. Jakubowski, M. Kobel, preprint DESY 89-165 (1989).
[26] F.A. Berends, R. Kleiss and S. Jadach, Nucl. Phys. B202 (1982) 63;
F.A. Berends and R. Kleiss, Nucl. Phys. B177 (1981) 237.
[27] F.A. Berends, P.H. Daverveldt and R. Kleiss, Comp. Phys. Comm. 40 (1986) 271, in a version without radiative corrections.

[28] J.A.M. Vermaseren, Nucl. Phys. B229 (1983) 347.
[29] M. Suffert, p-LEAR NOTE no. 41 (1979) unpublished.
[30] T. Sjøstrand, Comp. Phys. Commun. 43 (1987) 347.
[31] Z. Jakubowski et al., Z. Phys. C40 (1988) 49.
[32] Z. Jakubowski and S. Keh, CB Monte Carlo Progress Report, internal F31 note (1985) unpublished.
[33] W. Metzger, preprint HEN-278, Nijmegen (1987) unpublished.
[34] G. Mechtersheimer et al., Nucl. Phys. A324 (1979) 379; U. Klein et al., Nucl. Phys. A329 (1979) 339.
[35] C. Van der Velde-Wilquet et al., Nuovo Cimento 39A (1977) 538.
[36] J.B. Birks, The Theory and Practice of Scintillation Counters (Pergamon, Oxford, 1964).
[37] R.B. Murray and A. Meyer, Phys. Rev. 122 (1961) 815.
[38] G.T. Wright, Phys. Rev. 91 (1953) 1282.
[39] D. Blanc, F. Cambou and Y.G. de Lafond, C.R. Acad. Sci. 254 (1962) 3187.
[40] R. Gwin, Oak Ridge National Lab. Rep. ORNL 3354 (1962).
[41] R. Wigmans, High Resolution Calorimetry, invited talk given at Experimental Methods for Colliding Beam Physics, SLAC, USA, 1987.
[42] R. Aleksan and F. Pierre, preprint DPhPE 87-12 (1987).
[43] S.M. Shafroth, Response of Sodium Iodide to Neutrons, in: Scintillation Spectroscopy of Gamma Radiation (Gordon and Breach, London, 1967).